# The influence of turbulence on cycling aerodynamics

Christopher Brown*, David Burton, Timothy Crouch, Mark C. Thompson

*Fluids Laboratory for Aeronautical and Industrial Research (FLAIR), Department of Mechanical and Aerospace Engineering, Monash University, Melbourne, VIC 3800, Australia*

## Abstract

Many previous studies have focused on characterising Reynolds number effects and skinsuit design to better understand and improve aerodynamic performance. However, the majority of this research has been conducted in wind tunnels with turbulence intensities of less than 2%, considerably lower than that experienced when competing outdoors or in the wakes of competitors. In this systematic experimental study using passive turbulence generation, the influence of freestream turbulence on the aerodynamics of a cyclist is determined. Force measurements, wake velocity surveys, total pressure measurements and surface flow visualisations are used to characterise and quantify the aerodynamic behaviour. It is found that the aerodynamic drag is strongly affected by turbulence with it monotonically decreasing with increasing turbulence level. Moderate levels of turbulence are shown to alter local flow separation, and consequently the drag, on parts of the cyclist's body, which in turn is imprinted on the large-scale wake structures. The interaction of turbulence level and skinsuit roughness on the arms is also considered showing that these factors cannot be treated in isolation. Overall, this study highlights the importance of understanding the environment in which cyclists compete in order to optimise their performance.

*Keywords:* Cycling, aerodynamic, bluff body, turbulence, wind tunnel, drag.

## 1. Introduction

The past decade has seen considerable research into understanding the aerodynamic performance of cyclists. Equipment manufacturers have been continually innovating to develop new technology, and athletes are adopting refined positions to gain a competitive advantage over their competitors. Systematic studies have characterised the drag for varying postures (Barry et al., 2015a), as well as the positions (order) within a team pursuit (Barry et al., 2015b) or peloton (Blocken et al., 2018).

As athletes pedal, the changing geometry produces a complex, unsteady, highly three-dimensional flow field. Crouch et al. (2014) first considered in detail the importance of the large-scale flow structures in the wake of a cyclist, identifying several critical streamwise vortical systems forming from flow separation off the body. It was shown that the drag acting upon the cyclist was imprinted into these wake structures. Further to this, because of the difference between flow and pedalling timescales, Crouch et al. (2016) examined whether the wake could be treated quasi-steadily, i.e., whether a static-leg cyclist model approximately reflected the aerodynamic forces and wake associated with a pedalling cyclist at the same instantaneous pedal position. This confirmed the applicability of static leg mannequins. Typically, two leg positions are considered to analyse the extreme cyclic aerodynamic drag states of a cyclist. These correspond to a *symmetrical flow regime* (low drag) with the cranks close to horizontal and an *asymmetrical regime* (high drag) where the cranks are close to a vertical position.

In subsequent studies, Jux et al. (2018) and Terra et al. (2020) examined the flow fields of a static leg mannequin that was positioned in a more streamlined posture compared to the mannequin employed by Crouch et al. (2014). Using a robotic Particle Image Velocimetry system, Jux et al. (2018) characterised the vortex system in the wake.

*Corresponding author
*Email address:* christopher.brown@monash.edu (Christopher Brown)

Investigating the asymmetric leg position, it was found that significant streamwise vortex structures are generated from flow separation behind the hips, elbows, knees and feet. Following that, Terra et al. (2020) explored Reynolds number effects on the wake development. It was found that the near wake of certain (roughly cylindrical) limb sections featured typical bluff-body characteristics: two separating shear layers bounding a region of reverse flow. Specifically, the wake width of the lower leg and arm reduces with increased freestream velocity, following similar behaviour to an isolated cylinder passing through the drag crisis region. For this specific geometry, the critical Reynolds number of the arm and lower leg exceeded 25 $ms^{-1}$ (the maximum test speed), whereas regions across the knee were observed to undergo full transition. In contrast, the hip vortices were already immersed within a highly three-dimensional flow field. As Reynolds number was increased, the wake showed a stronger associated vortex structure and greater downwash due to later separation across the hip.

It has been proposed that reducing aerodynamic drag can be achieved by optimising surface textures on skinsuits covering the arms and legs of athletes (Brownlie et al., 2009). This relies on the theory of reducing the aerodynamic force by altering the flow separation behaviour in these regions. As well documented by Achenbach (1971, 1968), for spheres and cylinders, the aerodynamic force acting on the body depends on the attached/separating boundary-layer profile around convex surfaces. The laminar/turbulent state of this boundary layer is dependent on Reynolds number. For smooth surfaces, in the sub-critical regime, laminar separation occurs for $Re < 200\,000$, i.e., the boundary layer remains laminar prior to separation at $\approx 80°$. For Reynolds numbers $200\,000 < Re < 500\,000$ the attached and separating boundary layer undergoes significant change. The separated laminar boundary layer undergoes rapid turbulent transition allowing it to reattach to the surface forming a one or two-bubble flow state before again separating at a later point ($\approx 140°$). As a result, the wake width is reduced, and the drag acting upon the cylinder/sphere drops by a factor of up to 4 of that prior to transition. The Reynolds number associated with this dramatic drop in $C_D A$ is often referred to as the *Critical* Reynolds number (Achenbach, 1971).

The state of the boundary layer on a circular cylinder can be manipulated by adding surface roughness to certain regions. Through adding roughness early boundary layer turbulent transition can be induced, delaying boundary-layer separation and reducing pressure drag. This effectively causes onset to the critical flow regime at a lower Reynolds number. Zdravkovich (1990) discussed that surface roughness inhibits the formation of the separation bubble and eliminates the one and two-bubble regimes. Depending on the size and shape of the roughness elements, the post-critical regime is strongly affected. As Reynolds number increases, the frictional resistance increases as excrescences on the surface are exposed and boundary layer momentum decreases. Consequently, the minimum drag increases but occurs at a lower Reynolds number, a phenomenon that can be used in a targeted way.

Flow conditions a cyclist may experience when competing on a track or outdoors covers a wide range. Fitzgerald et al. (2019, 2022) measured turbulence intensity for cyclists competing in track events: individually, in a bunch race with 16 competing riders, and in a team pursuit. By taking 3-component velocity measurements with a four-hole pressure probe attached to the front of the bike, he found that a cyclist experienced 1.0% and 2.6% turbulence levels over a 6-lap average when competing solo or within a bunch race, respectively. When riding within the team pursuit, a rider in position 2, 3 or 4 could experience turbulence intensities up to 14.9%, 17.3% and 18.5%, respectively. Beyond this, environmental conditions can vary significantly when competing in an outdoor time trial; however, limited research has been published on cyclists competing outdoors. Of relevance to this study, for vehicle aerodynamics, Wordley and Saunders (2009) measured the background turbulence for a range of on-road environments. It was found that across environments, including city canyons, smooth terrain and road-side obstacles, turbulence intensity varies significantly between 2% and 16%. Interestingly, a cyclist travels at significantly slower speeds and with variance of the signal not changing, the turbulence intensity will be much higher. Despite this, almost all cycling aerodynamic research has been conducted in low-turbulence environments. Wind-tunnel investigations have covered a range of turbulence intensities from ~0.2% (Blocken et al., 2018; Defraeye et al., 2014)), ~0.8% (Jux et al., 2018; Terra et al., 2020) to ~1.6% (Crouch et al., 2014; Brown et al., 2020). The effect of turbulence on both streamlined and bluff-body aerodynamics has been well documented and can significantly impact aerodynamic performance.

The flow past a cyclist leads to a complex separated wake. Increasing turbulence levels can change the properties of both the attached boundary-layer flow and the separating shear-layer behaviour. An increase in turbulent fluctuations within the free-stream perturbs flow separation. It can also increase momentum transfer across the shear layer (Khabbouchi et al., 2014) and cause more significant entrainment into the wake (Bearman and Morel, 1983).

In fact, increasing the turbulence within the flow has a similar effect to increasing surface roughness (Sadeh and Saharon, 1982; Blackburn and Melbourne, 1996). Turbulence can enhance the magnitude and angular extent of the

favourable pressure gradient region and can result in a delayed separation of up to 140° (Sadeh and Saharon, 1982). The effective result is that the flow is pushed into the behaviour seen at higher Reynolds number resulting in an early transition to the post-critical regime (Blackburn and Melbourne, 1996). This can reduce drag on bodies that would otherwise lie within the sub-critical regime to between 3% and 54% (Sadeh and Saharon, 1982). Khabbouchi et al. (2014) supported this by showing a corresponding reduction in wake size as turbulence intensity is increased, as the opposing separated shear layers move closer together to narrow the wake. It has also been shown that spheres see similar effects to cylinders with increasing turbulence levels (Kwangmin et al., 2010). More recently, Burton et al. (2021) demonstrated that with increasing turbulence levels increased the switching rate of the bi-stable state of asymmetric wakes of square-back vehicles.

The varying turbulence levels relevant to many cycling events, together with evidence suggesting that it matters, has motivated this research. This experimental study investigates a mannequin's aerodynamic performance and the associated flow field over a range of turbulent conditions between 1% and 10%. Turbulence was generated in a wind-tunnel through passive grids paired with modifications to its flow contraction to vary the oncoming flow in which the cyclist model was positioned.

We will show that the aerodynamic drag acting on a cyclist changes significantly with increasing levels of turbulence and that this is strongly reflected in the wake dynamics. Through comparisons of velocity and total pressure fields in cross-sectional planes in the near wake, we will highlight the breakdown of large-scale vortices with increasing turbulence levels and a reduction in wake cross-sectional size. This will be shown to be linked to the local flow states across critical parts of the mannequin geometry. We will also show the influence of turbulence on the aerodynamic performance of a mannequin dressed in a Lycra skinsuit with surface roughness added to the arms, to establish the analogous effects of upstream turbulence and surface roughness.

## 2. Experimental setup

### *2.1. Wind Tunnel*

All experiments were undertaken in the Monash Large-Wind-Tunnel Facility located at Monash University, Australia. The large wind tunnel is a return-circuit design with a 3/4 open-jet test section. The open-jet test section has the useful capability that the jet can be configured at two heights, which affects flow velocity and oncoming turbulence level, as discussed later. The standard configuration has a test section size of 12×4×2.6 m ($L \times W \times H$), and the second configuration is $12 \times 4 \times 4$ m. A schematic diagram of the wind tunnel is presented in figure 1, showing the location of the cyclist mannequin in the test section. A Pitot-static tube upstream of the cyclist and downstream of the contraction was used to calculate a reference velocity. A dynamic pressure correction was applied from the reference Pitot-static tube to the stagnation point height on the cyclist's helmet (determined without the presence of the mannequin in the test section). An array of 6 Pitot-static tubes were located upstream of the contraction and any passive-turbulence generators as a secondary speed calculation. The free-stream velocity was controlled by changing the speed of the two fixed pitch 5 m diameter fans. Further details are provided in previous studies Crouch et al. (2014); Bell et al. (2016).

A range of quantitative and qualitative experimental techniques were used to characterise the influence of turbulence on a cyclist. The techniques included force measurements, velocity wake surveys, total pressure wake measurements and surface flow visualisation covering a range of turbulence intensities.

### *2.2. Turbulence generation*

Passive techniques were utilised to generate varying turbulence intensities. As outlined above, the wind tunnel was configured with two separate jet heights, 2.6 m and 4.0 m. Upstream of the contraction, the wind tunnel has in-built flow conditioning screens positioned after the fans. These screens can be opened to help increase the amount of turbulence within the flow.

Overall, three parameters are used to control the turbulent flow state: the jet height, flow conditioning screens and the grid configuration. Primarily, turbulence levels in the test section were increased by passive grid generators. The grid configurations were mounted 11 m upstream of the cyclist and 1 m upstream of the beginning of the contraction. A schematic of the grid setup is provided in figure 2. H1-4 represents a horizontal slat, and V1-2 represents a vertical slat within the grid configuration, with $D$ being the associated diameter (mm) of each slat. The location of each slat relative to one another and to the wind tunnel walls is detailed in figure 2. Due to the non-linearity of turbulence generation

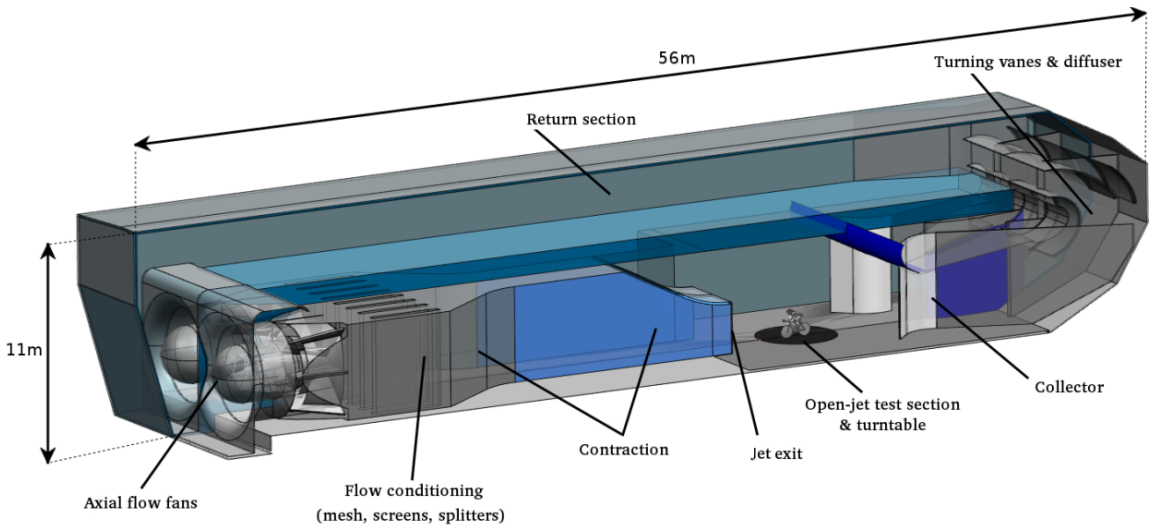


**Figure 1:** Monash Large Wind Tunnel schematic diagram. (Crouch et al., 2017)

through a contraction, a mixture of slat dimensions was utilised to generate approximately uniform turbulence and uniform velocity profiles. This was done through a trial and error process, with adjustments performed until the profiles were deemed satisfactory. Table 1 provides detailed information on the different configurations together with the induced velocity and turbulence properties.

To characterise the levels of turbulence that the cyclist experiences, unsteady velocity profiles were measured in an empty tunnel. Four-hole dynamic pressure probes, also known as *'Cobra probes'*, referred to herein as a probe, were used to measure the velocity field in a cross-sectional plane at the location of the front wheel. These probes measure three velocity components within a $\pm 45^o$ acceptance cone, More details of the methodology are provided in recent publications (Crouch et al. (2014); Bell et al. (2016); Avadiar et al.) where probes have been used to characterise boundary layers and the wakes of bluff bodies. The probe pressure transducers have a frequency response of up to 2000 Hz and were sampled at 8000 Hz. The free-stream turbulence was quantified by the turbulence intensity and length scale. The strength of the turbulence is defined by the turbulence intensity, shown in equation 1, whereas the length scale is a statistical representation of the spatial dimension of the most energetic turbulent structures. The turbulence intensity, $I_i$, is a non dimensional ratio of the root-mean-square velocity fluctuations to freestream velocity:

$$I_i = \frac{\overline{(u_i' u_i')}^{\frac{1}{2}}}{U_\infty}, \qquad i = \{x, y, z\} \tag{1}$$

where $u_i' \in (u', v', w')$ are the fluctuating velocity components of streamwise ($x$), lateral ($y$) and vertical ($z$) components, and $U_\infty$ is the free-stream velocity. Throughout this study, unless otherwise stated, the term *turbulence intensity* relates to the streamwise component, $I_x$, only.

The normalised velocity and turbulence profiles across each configuration are shown in figure 3. The normalised velocity distributions highlight that the turbulence generation methods alter the boundary layer to different extents. The boundary layer profiles show some variation across the range of turbulence intensities with a maximum 99% height of 500 mm when the flow condition screens are open with the jet down and no grids positioned in the tunnel. An integral average of velocity between 500 mm and 1300 mm was used to calculate the reference velocity $U_\infty$. This region is predominantly outside the floor boundary layers across all configurations and is the range between the minimum and maximum height of the mannequin. This region was used to calculate the turbulence intensities and length scales provided in table 1. The turbulence profiles across the mannequin height have excellent uniformity. The maximum variation as quantified by the variance about the mean between 500 mm and 1500 mm is 1.1%.

This study used a common approach to fit the data to a von-Kármán spectrum to characterise the turbulent length scale. The von-Kármán spectrum, defined through equations 2a and 2b, determine the turbulent length scales $L_x$, $L_y$, $L_z$

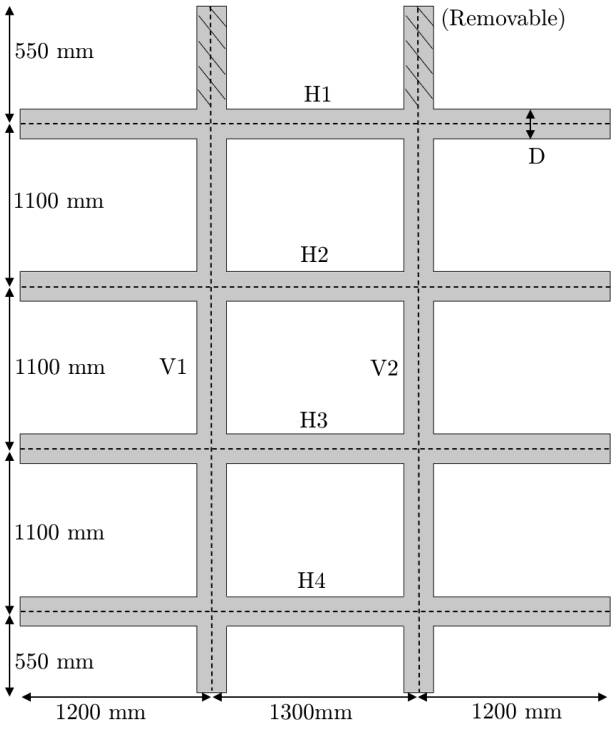


**Figure 2:** Schematic diagram of the grid configuration used to generate turbulence, which was positioned upstream of the contraction.

based upon an empirical fit of normalised streamwise and cross-stream power spectra of the velocity (von Kármán, 1948):

$$\frac{f P_{xx}}{\sigma_u^2} = \frac{4 L_x f_x}{U_\infty} \frac{1}{(1 + \frac{1.339 L_x 2\pi f_x}{U_\infty})^{\frac{5}{6}}}, \tag{2a}$$

$$\frac{f P_{ii}}{\sigma_i^2} = \frac{4 L_i f_i}{U_\infty} \frac{1 + \frac{8}{3}(\frac{2.678 L_I 2\pi f_i}{U_\infty})^2}{(1 + (\frac{2.678 L_i 2\pi f_i}{U_\infty})^2)^{\frac{11}{6}}}, \qquad i = (y, z). \tag{2b}$$

The power spectra for this study were obtained by using Welch's method, splitting the data sets into 1 s segments with 50% overlap and applying Hamming windows to reduce side-bands. Approximating each data set to von Kármán (1948) spectra based on least squares regression fits up to a frequency of 400 Hz, allowed the three length scales, $L_x, L_y, L_z$, to be extracted. This restriction of 400 Hz was due to the Cobra probe only being able to accurately capture a reduced range of frequencies due to the physical size of the probe head. Shown in figure 4 are the least squares regression fits for a freestream turbulence intensity of 3.6% at the stagnation height of the cyclist. Here, the Power Spectral Density ($f\ P_i$) was normalised by the variance of the signal $\sigma_i^2$.

The setup enabled a parametric study of turbulence intensity effects, over the range of 1.4% to 9.1%. Whilst the length scale was measured, it was not controlled, and for all cases, $L_x$ was in the range of 0.11 m to 0.41 m. The combined data set spans most of the range of turbulence intensities experienced by on-road vehicles (Wordley and Saunders, 2009) and under track conditions Fitzgerald et al. (2019), as discussed above. However, the length scales are smaller than those identified by Wordley and Saunders (2009) for on-road conditions, but are perhaps more appropriate for turbulence caused mostly by upstream cyclists, rather than larger vehicles and surrounding buildings and vegetation.

| Jet (m) | $D_{H1,H2}$ | $D_{H3,H4}$ | $D_{V1,V2}$ | Screens | $I_x(\%)$ | $I_y(\%)$ | $I_z(\%)$ | $L_x$ (m) | $L_y$ (m) | $L_z$ (m) |
|---|---|---|---|---|---|---|---|---|---|---|
| 2.6 m | N/A | N/A | N/A | Closed | 1.4 | 1.8 | 1.8 | 0.16 | 0.36 | 0.26 |
| 4.0 m | N/A | N/A | N/A | Closed | 2.5 | 2.8 | 2.3 | 0.20 | 0.19 | 0.11 |
| 4.0 m | N/A | N/A | N/A | Open | 3.6 | 3.4 | 3.5 | 0.26 | 0.17 | 0.13 |
| 2.6 m | 0.2 m | 0.1 m | 0.2 m | Closed | 5.4 | 5.3 | 5.6 | 0.19 | 0.15 | 0.15 |
| 4.0 m | 0.2 m | 0.1 m | 0.2 m | Closed | 7.8 | 7.0 | 6.4 | 0.28 | 0.15 | 0.11 |
| 4.0 m | 0.2 m | 0.2 m | 0.2 m | Closed | 9.1 | 7.3 | 7.1 | 0.41 | 0.13 | 0.13 |

**Table 1:** Wind-tunnel turbulence properties and configuration parameters for each turbulence intensity.

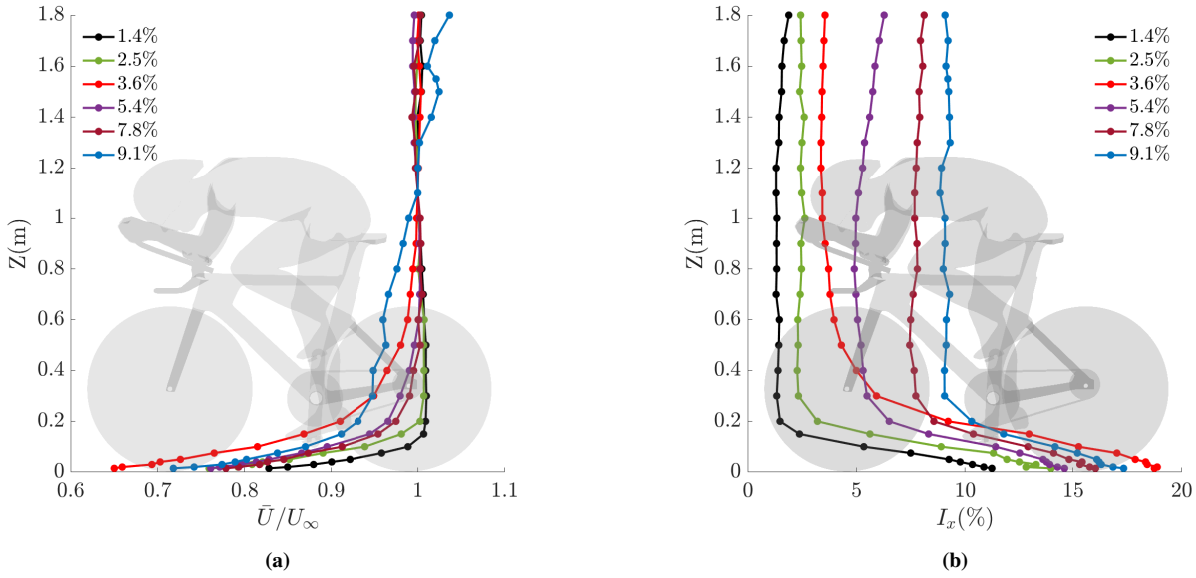


**Figure 3:** Boundary layer profile at the centre of the front wheel for each freestream turbulence intensity: **(a)** normalized velocity, $U^*$ **(b)** streamwise turbulene intensity, $I_x$.

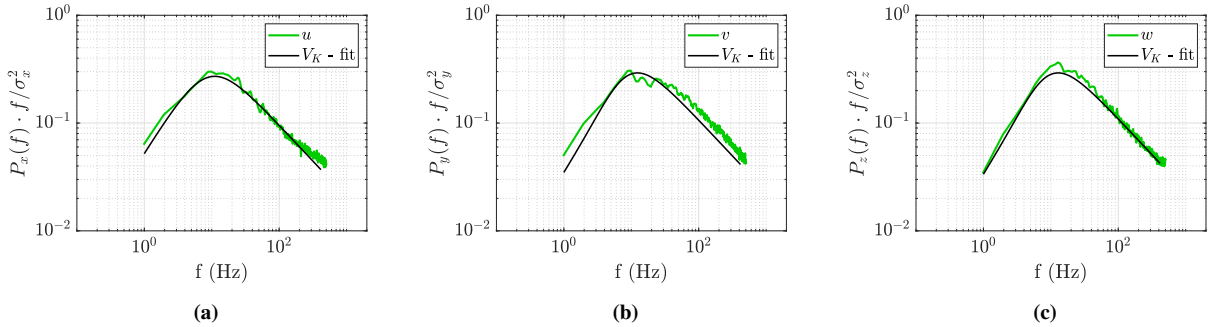


**Figure 4:** Illustration of length-scale calculations based on fitting von-Kármán spectra for a freestream turbulence intensity of 3.6% for: **(a)** streamwise velocity ($u$), **(b)** lateral velocity ($v$), **(c)** vertical velocity ($w$).

| Name | Symbol | Position/Length |
|---|---|---|
| Hip angle | $\beta$ | $16^o$ |
| Elbow angle | $\alpha$ | $19^o$ |
| Torso angle of attack | $\gamma$ | $8^o$ |
| Chord length | c | 650 mm |
| Should Width | sw | 470 mm |
| Hip Width | hw | 350 mm |
| Crank Length | cl | 175 mm |
| Wheel Base | wb | 950 mm |
| Wheel Diameter | wd | 622 mm |

**Table 2:** Mannequin and bicycle characteristic lengths and angles. Definitions are provided in figure 5.

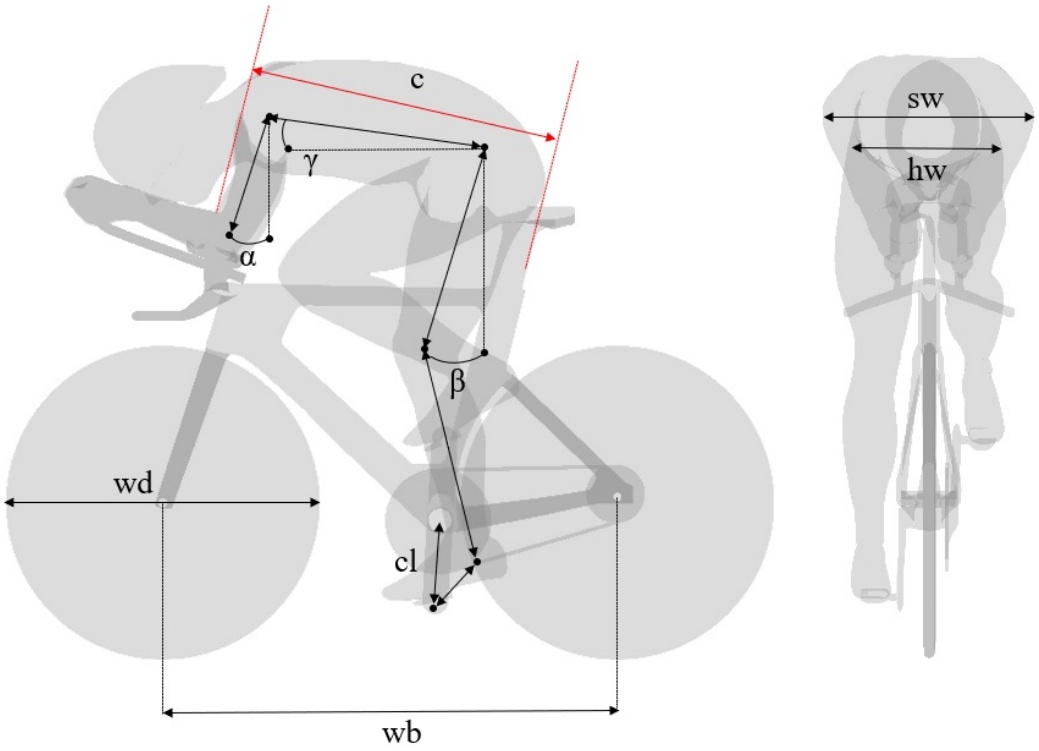


**Figure 5:** Schematic mannequin geometry in the vertical leg position.

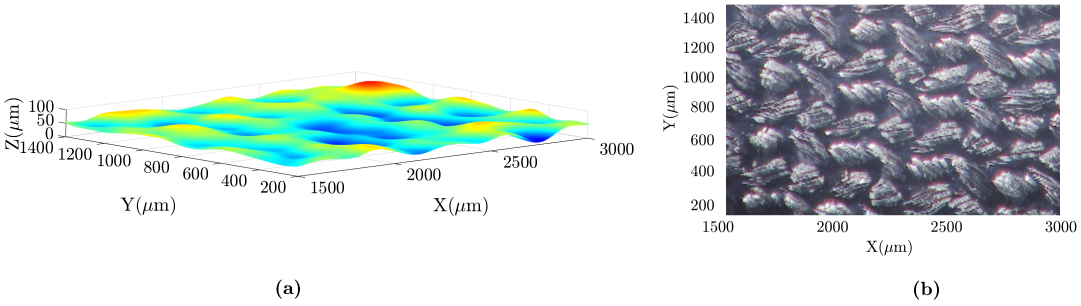


**Figure 6:** Lycra fabric characterisation of the skin suit: **(a)** Two-dimensional roughness height profile of the lycra material; and **(b)** A microscope image showing the details of the weave.

### *2.3. Cycling mannequin*

The mannequin used for this study is representative of a de-identified elite-level cyclist in the pursuit position obtained through 3D scanning of athletes. The mannequin was a machined foam model covered in a hard-setting smooth-surface epoxy resin. It was mounted onto a modern, commercially available track bike frame with two off-the-shelf disc wheels and was equipped with a medium helmet and track shoes for all configurations. The research was conducted with the legs of the mannequin positioned vertically at $\sim 90^o$ – the asymmetric leg position – corresponding to the high drag position. The 0° leg position – the asymmetric leg position – corresponds to the mannequin positioned with the legs approximately horizontal. That position was not considered in this study. Figure 5 provides a schematic of the setup with key parameters labelled and parameter values presented in table 2. The mannequin geometry was the same as that used in the computational study conducted by Wang et al. (2022). The frontal area for the vertical leg position was 0.351 m. The mannequin was configured as *bare* or with *skinsuit*. The *bare* configuration is set up to be aerodynamically smooth over its entire surface. The *skinsuit* configuration indicates that the mannequin is dressed in a skinsuit made from a Lycra material, but with different stitching, and therefore roughness, on the arms. The lycra material has a mean thickness of $\sim 0.4$ mm. The skin suit has seams joining the arm roughness, and also in the groin region where padding is stitched into the suit. The roughness and stitching style of the skinsuit is shown in figure 6 where the average and standard deviation of the roughness across a $2 \times 3$ mm area is $0.068 \pm 0.0028$ mm. The arm roughness consists of regular ridges uniformly spaced 10 mm apart covering the entire arms. A view of the "roughness" on the arms of the mannequin wearing the skinsuit is provided in figure 7b.

### *2.4. Force Measurements*

Time-average aerodynamic forces were measured during the testing. Forces acting on the mannequin/bike combination were measured using a six-component Kistler force balance of the piezoelectric type that was calibrated before force measurements. The measurement system includes four individual three-component piezoelectric force transducers that output three force components and associated moments. As outlined in Crouch et al. (2014), the combined uncertainty of the entire drag for this type of measurement system is of the order of $\pm 0.565N$ – typically within 1.5%. Further details of the Kistler force setup can be found in Cam (2008). The mannequin and bike were connected to the force balance through struts connected to the front and rear axles. The force balance was housed within a false floor with an extended splitter plate used to reduce the influence of the wind-tunnel boundary layer. Each force measurement was a time-averaged result of a 90-second sample at 500 Hz. Each test also involved a zero windspeed measurement before and after the force measurement to account for any drift in the system over the test duration. The maximum drift recorded for any given test, normalised by the mean was 1.26%, and the mean drift across all measurements was 0.33%. Force results presented in this study are shown as forces coefficient areas, $C_d A$ $(m^2)$and $C_L A$ $(m^2)$, and are

calculated based upon:

$$C_D A = \frac{D}{\frac{1}{2}\rho U_\infty^2}, \tag{3a}$$

$$C_L A = \frac{L}{\frac{1}{2}\rho U_\infty^2}, \tag{3b}$$

where $D$ is the drag force, $L$ is the lift force, $\rho$ is the air density and $U_\infty$ is the free-stream velocity.

### 2.5. Velocity field measurements

Detailed three-component velocity wake measurements were taken 0.6 m behind the mannequin for each turbulence configuration. A two-axis traverse system was used to position two 4-hole probes to gridded measurements locations in the wake. The two probes were situated 150 mm apart and were fixed to a carbon fibre rod that extended 0.7 m out from the horizontal axis, far enough that there was minimal interference from the traverse system. The setup is shown in figure 7a. The traversed area was 1 m × 1.3 m. Probe measurements were recorded at evenly spaced intervals of 0.025 m in both the vertical and horizontal directions, as depicted in figure 7c. The coordinate system adopted follows the convention where $\{x, u\}$, $\{y, v\}$ and $\{z, w\}$ correspond to the streamwise, spanwise and vertical directions and velocity components. All wake surveys were taken at 16 ms$^{-1}$, a representative race speed for elite cyclists. Using the gridded velocity field, time-averaged vorticity fields were calculated, presented as normalised streamwise vorticity, $\omega_x$:

$$\omega_x = (\nabla \times \vec{V})_x \left(\frac{L}{U}\right), \tag{4}$$

where $L$ is the chord length of the mannequin shown in figure 5, and $\vec{V} = (u, v, w)$ is the local velocity vector.

Vorticity characterises the local rotation rate of the fluid; however, by itself it is not suitable for identifying the location or extent of a *vortex* structure. In this study, the $\Gamma_2$ criterion (Graftieaux et al., 2001) is used to identify the bounds of the vortex. The $\Gamma_2$ measure is a Galilean invariant scalar quantifying the rotation of a fluid over a region of interest. Similar to the $Q$ criterion (Hunt et al., 1988), it measures the excess of rotation rate over strain rate, although over a specific plane of interest. The bounds of a vortex structure depends on a chosen threshold, and Graftieaux et al. (2001) suggests that a limit of $\Gamma_2 = 2/\pi$ is suitable since that is the lower limit beyond which the flow is locally dominated by rotation. This value is adopted for this study. The circulation is defined by:

$$\Gamma = \oint_C \vec{V} \cdot d\vec{l}. \tag{5}$$

The *strength* of each vortex was identified by the circulation calculated by this equation (5). The boundary is based upon the $\Gamma_2$ criterion as discussed by Graftieaux et al. (2001) (and above).

### 2.6. Total pressure grid

Pressures were recorded on an array of 117 total probe locations in the $Y$–$Z$ plane, situated 0.6 m behind the rear of the mannequin. A photo of the total pressure grid setup can be seen in figure 7b, with measurement locations highlighted in figure 7c. The total pressure grid measured the time-average and fluctuating total pressures across the Reynolds number range of interest. This enabled the identification of fundamental wake dynamics across a range of wind speeds. The probe measurement locations were equally spaced 80 mm apart in a grid arrangement with each probe connected to a 128-channel *Differential Pressure Measurement System* (DPMS). The tubing length was 1500 mm with a 1.5 mm inner diameter allowing a frequency response of 150 Hz after correction for the phase and amplitude based on the length and diameter of the tubing. The pressure, $P_i$, measured at each probe was converted to a pressure coefficient, $C_P$, based on

$$C_P = \frac{P_i - P_s}{P_t - P_s}, \tag{6}$$

where $P_t$ is the total pressure and $P_s$ is the static pressure measured by the upstream reference Pitot-static tube. A static pressure correction was applied based on the relationship between the static pressure at the upstream pitot and the static pressure in the centre of the test rig with nothing inside the tunnel.

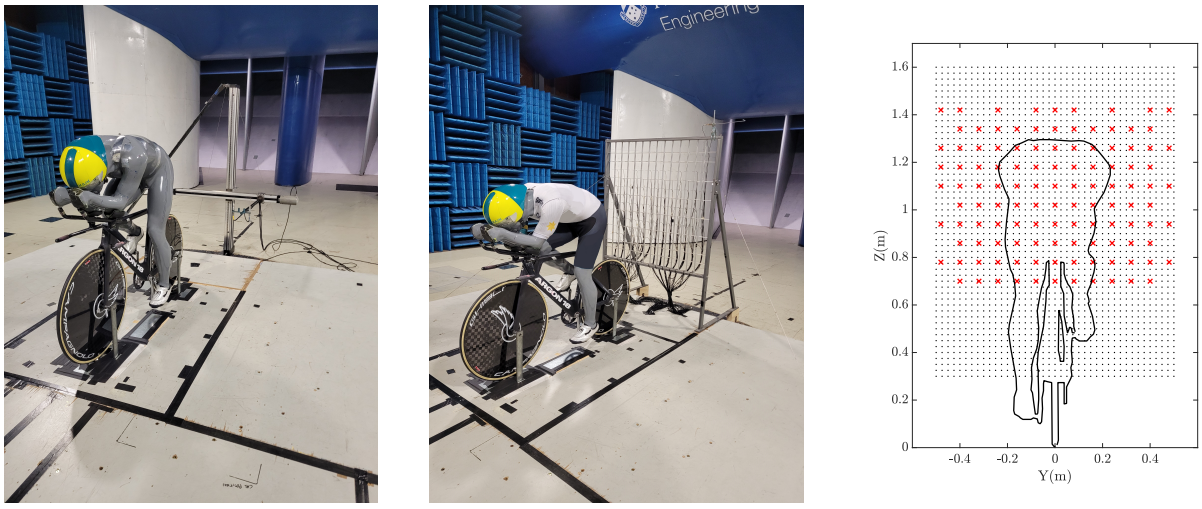


**(a)** **(b)** **(c)**

**Figure 7:** **(a)** Traverse set up in the wake of the bare mannequin. **(b)** Total pressure grid in the wake of the mannequin dressed in a skinsuit. **(c)** Measurement locations at 0.6 m behind the rear of the mannequin. Here, × = total pressure grid; · = four-hole probe locations.

A pitot static tube was positioned at the grid location off to one side for further correlation of the static and total pressure. It is important to note that the total pressure grid was a source of blockage in the wake of the model. To assess its impact on the aerodynamics, mannequin force measurements were compared with and without the grid in place across each turbulence configuration. It was found to induce a constant $C_D A$ offset of $\sim$0.0105 $\pm$0.0014, which did not change with Reynolds number. This implies a constant base pressure offset due to the presence of the grid. Empty tunnel measurements of the pressure gradient in front of the total pressure grid confirmed this, with an increase in the static pressure coefficient of $\sim$4% when compared to the no-total-pressure-grid setup.

### *2.7. Flow visualisation*

In an attempt to visualise the time-average skin-friction, surface flow visualisations were undertaken on the mannequin at two turbulence intensities: 1.4% and 9.1%. A mixture of kerosene, fluorescent pigment, china clay and linseed oil was sprayed over the mannequin using a pressurised spray gun at low wind speeds. The wind tunnel speed was ramped up to 22 ms$^{-1}$, then maintained until the mixture was essentially dry. Due to the highly 3-dimensional geometry of the mannequin, the patterns presented were influenced by gravity and flow-field characteristics. To better understand the flow physics, segments of the mannequin were sprayed individually to ensure the wall shear stress was the dominant mechanism over gravity. The higher wind speed of 22 ms$^{-1}$ also provided more reliable results due to increased flow momentum to reduce the influence of gravity. Photographs were taken under UV light to enhance the fluorescent pigments on the surface of the mannequin. Following the flow visualisation analysis presented in Crouch et al. (2014), separation lines, surface streamlines and critical points were extracted.

## 3. Results

### *3.1. Introductory remarks*

Presented below are results for the five different freestream turbulence levels, herein referred to by $I_x$, for each mannequin configuration. The maximum blockage ratio for any test was 3.3%. Corrections were investigated based upon techniques presented by Mercker et al. (1997), which considers the model's blockage ratio and volume, the proximity of the model to the nozzle exit and collector, and the static pressure variation in the test section. Across the test section, the maximum variation in static pressure coefficient was $C_{p,stat} \pm 0.02$. Applied to the estimates provided

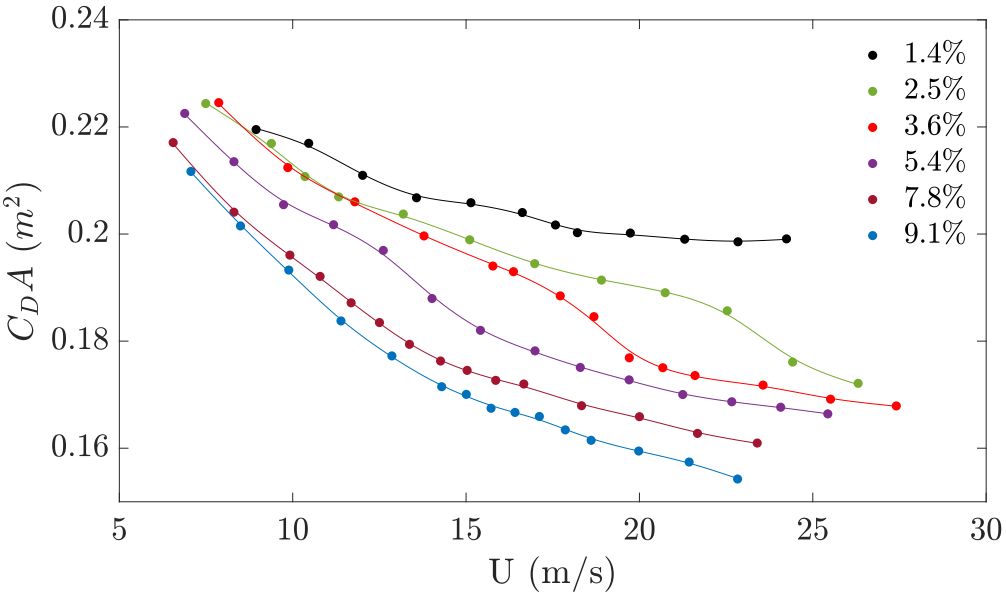


**Figure 8:** Drag area, $C_DA$ ($m^2$), versus wind speed for turbulence intensities between 1.4% and 9.1%.

by Mercker et al. (1997), the maximum corrections to force and pressure coefficients were < 0.6%. Thus, this was considered a (small) secondary effect and therefore no corrections were made.

An in-depth analysis of the influence of turbulence on the bare mannequin in the 90-degree leg position is presented in section 3.2. This includes analysis of the force measurements, wake profiles, total pressure profiles, and flow visualisation to highlight aerodynamic changes across the turbulence level and Reynolds number. An analysis of the 90-degree leg position with the mannequin wearing a skinsuit is given in section 3.3.

### *3.2. Bare Mannequin – 90-degree leg position*

#### *3.2.1. Force results*

The drag area, $C_dA$ ($m^2$), as a function of wind speed ($ms^{-1}$) is presented in figure 8. Although cyclists do not often travel at speeds > 25 $ms^{-1}$, the velocity sweeps were extended beyond standard cycling speeds to gain insight into a broader range of aerodynamic phenomena across each $I_x$ level. Importantly, there is a general reduction in $C_DA$ with increasing turbulence levels and the quantum of this reduction is higher as the Reynolds number is increased. For the high turbulence case, drag is reduced by as much as 22% relative to the low turbulence case. This is perhaps surprising, as it is an extremely large change and, therefore, of great significance to the aerodynamic performance of cyclists. It is clearly important to understand the underlying mechanisms.

At the lowest wind speeds (< 10 $ms^{-1}$), there is a reduction in $C_DA$ with increasing turbulence level. Over this range, $C_DA$ decreases approximately linearly with wind speed, with the gradient becoming larger as $I_x$ is increased. Between wind speeds 10 $ms^{-1}$ < $U$ < 20 $ms^{-1}$, the behaviour is more complex and a strong function of turbulence intensity. Beyond 20 $ms^{-1}$, there is a significant difference in $C_DA$ with increasing $I_x$. At a wind speed of 16 $ms^{-1}$, for $I_x$ = 1.4%, $C_DA$ is approximately 0.204, whereas at the highest $I_x$ = 9.1%, the minimum $C_DA$ is approximately 0.166 – a 19% reduction.

At $I_x$ = 2.5%, an inflection point is evident with a change in the second derivative of $C_DA$ versus wind speed occurring at ~ 23 $ms^{-1}$. This is associated with a rapid reduction in $C_DA$ of 5.5% between 23 $ms^{-1}$ and 25 $ms^{-1}$. At $I_x$ of 3.6%, this reduction begins at approximately 18 $ms^{-1}$, and at 13 $ms^{-1}$ when $I_x$ is 5.4%. This is indicative of a fundamental change to the flow over the cyclists, in particular, it is consistent with parts of the mannequin undergoing the drag-crisis transition. The trend is seen for other curved bluff bodies, where increased upstream turbulence leads to boundary-layer transition and delayed separation at lower Reynolds numbers (Achenbach (1971); Blackburn and

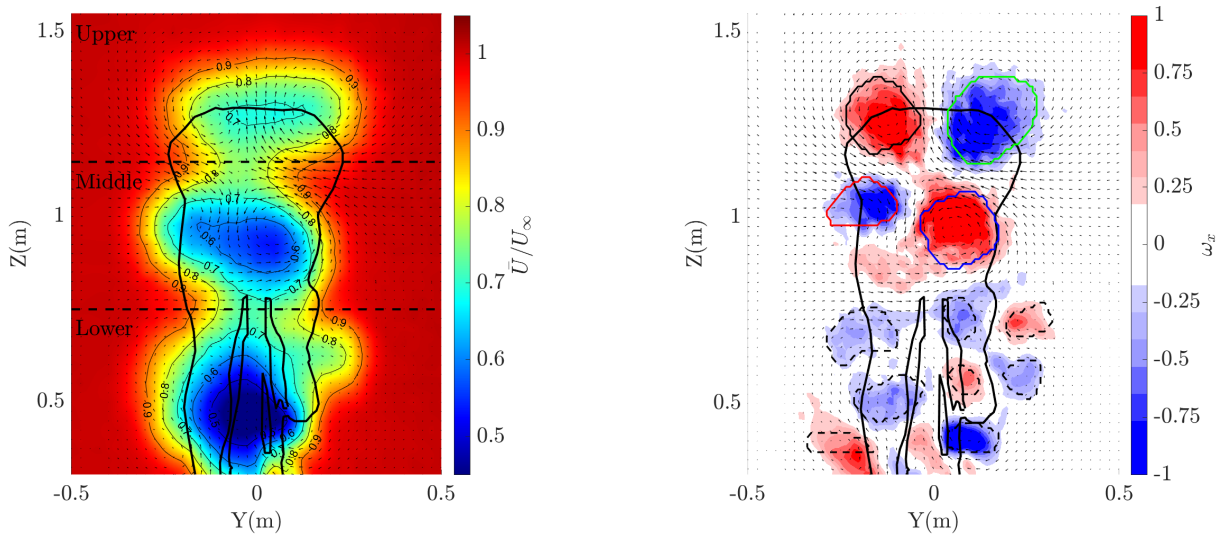


**Figure 9:** Wake contour maps: **(a)** $U^*$, and **(b)** $\omega_x$, 0.6 m behind the bare mannequin for the baseline $I_x = 1.4\%$ case. Key large-scale structures are highlighted: — = left elbow, — = right elbow, — = left hip, — = right hip, – – = lower wake structures.

Melbourne (1996); Khabbouchi et al. (2014)). Interestingly, this rapid drag-area drop is not apparent for the two highest turbulence level cases, i.e., for $I_x \geq 7.9$, the $C_DA$ curves show no sudden reduction occurring. This will be further discussed in the following sections.

### 3.2.2. *Baseline wake topology*

To better understand the cause of the reduction in drag with increasing turbulence, wake velocity profiles were taken at 16 ms$^{-1}$ across all $I_x$ levels. We first consider the baseline condition (lowest turbulence case), $I_x = 1.4\%$, for which dominant flow structures are evident. The flow speed contour plots shown in figure 9a present a cross-section through the wake at $x = 0.6$ m. It shows three distinct regions: the upper region (labelled Upper), middle region (Middle) and lower region (Lower). Each of these regions displays a local velocity minimum. In the upper section of the wake, the minima is within the isoline of $U^*$ ($= \overline{U}/U_\infty$) $= 0.7$; for the mid-wake it is inside the isoline $U^* = 0.6$; and in the lower wake the velocity minima is within the isoline of $U^* = 0.5$. Figure 9b shows a contour map of the corresponding normalised vorticity, $\omega_x$. From this it is seen that the local velocity deficits are connected with large-scale swirling structures in the wake.

In the upper region, there is a pair of counter-rotating vortices. The boundary of each structure, identified by $\Gamma_2 = 2/\pi$, is highlighted by a solid black and green line for the left and right vortices, respectively. These structures are formed from flow separation from either elbow and pulled into the upper wake, as shown through numerical simulations (Wang et al., 2022) for the same geometry. They are also similar to those presented in Crouch et al. (2014) and Jux et al. (2018). This will be examined in more detail later using surface oil visualisations. In the mid-section of the wake, there is another pair of counter-rotating vortices, the left and right hip vortices, these are shown by the red and blue solid lines in figure 9b, respectively. These have been well documented in research (Wang et al., 2022; Terra et al., 2020; Crouch et al., 2014) as the hip vortices and are often the strongest large-scale vortical structures generated behind a cyclist. Here, these are of a similar size and peak vorticity to the elbow vortices. For this leg position, the left hip vortex is smaller and slightly higher than the right hip vortex, aligning with the shape of the mid-wake velocity contours. A combination of smaller vortical structures are formed in the lower wake, all highlighted by dashed black lines. These include the left shank and foot vortex on the outstretched leg, as well as the tucked right knee and right foot vortex pair. These are similar to those found by Jux et al. (2018) and Terra et al. (2020).

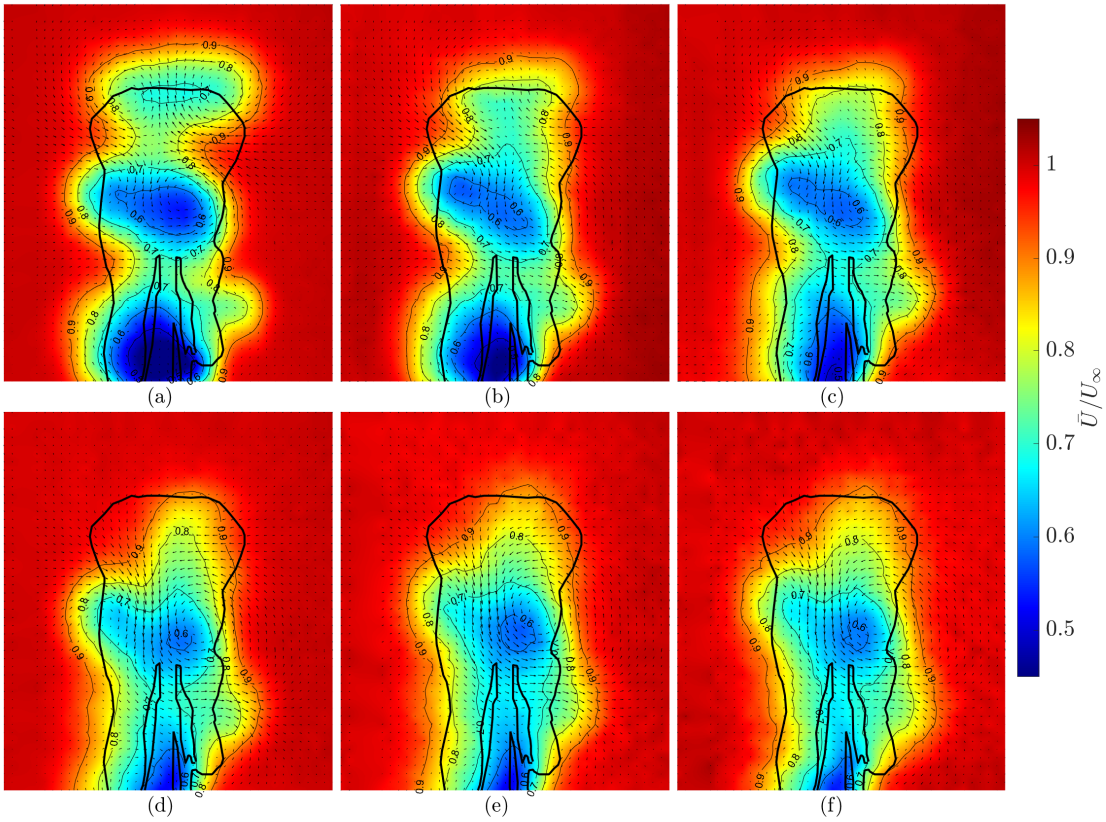


**Figure 10:** Normalised velocity contour maps, $U^*$, 0.6 m behind the mannequin at a wind speed of $U_\infty = 16$ ms$^{-1}$ for **(a)** 1.4%, **(b)** 2.5%, **(c)** 3.6%, **(d)** 5.4%, **(e)** 7.8% and **(f)** 9.1%.

### *3.2.3. Wake flow topology changes subject to turbulence*

We now consider how increased freestream turbulence affects the distribution and magnitude of the wake velocity and vorticity. Of particular importance are changes to the salient structures (elbow and hip vortices) that were identified above for the baseline case and the connection of these to the observed drag variation. Figures 10 and 11 show $U^*$ and $\omega_x$ contour maps over the range of freestream turbulence intensities generated. Solid and dashed lines highlight the boundaries of both the key large-scale structures and the minor smaller-scale structures, the same as those presented in figure 9b. Figure 12 characterises the vortex strength, based on the circulation given by equation 5, and the area of each large-scale structure across the range of freestream turbulence intensity considered.

For an increase in turbulence intensity to $I_x = 2.4\%$, there are only minor changes to the wake profiles. The left and right elbow vortices in the upper wake are weaker and have a smaller associated area (figure 10b). This is consistent with changes to the localised velocity deficit in that area, including a reduction in wake width and velocity, with $U^* > 0.7$. Figure 12 shows that the right elbow vortex strength and size are reduced significantly. The mid and lower wake have reduced areas associated with $U^* < 0.6$. The minor structures formed off the right tucked knee have merged into a single vortex pair. The reduced wake size and deficit, and lower vorticity in the upper region explain the drag reduction for this case.

At $I_x = 3.6\%$, there are only minor changes in the near wake structures. Figure 10c shows a slight reduction in the upper-wake deficit with the $U^* = 0.9$ and $U^* = 0.8$ isolines moving closer together. The associated elbow vortices decrease in strength, whilst remaining similar in size. For higher turbulence levels, it is probable that the free shear layers experience higher levels of entrainment from the free-stream turbulence. Although the elbow vortices can still be observed (figure 11c), their strength is reduced when compared to the lower turbulence levels. The mid-

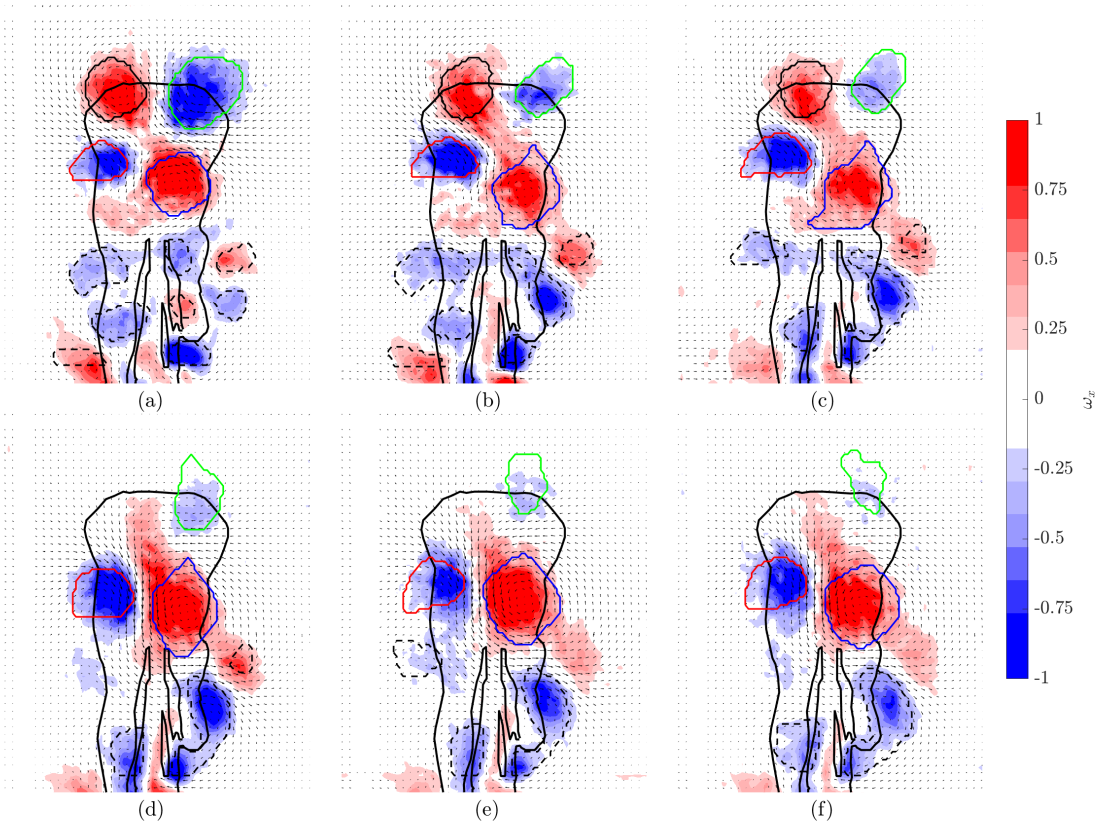


**Figure 11:** Normalised vorticity contour maps showing $\omega_x$, at 0.6 m behind the mannequin at a wind speed of $U_\infty$ = 16 ms$^{-1}$ for **(a)** 1.4%, **(b)** 2.5%, **(c)** 3.6%, **(d)** 5.4%, **(e)** 7.8% and **(f)** 9.1%. Key large-scale structures are highlighted: — = left elbow, — = right elbow, — = left hip, — = right hip, – – = lower wake structures.

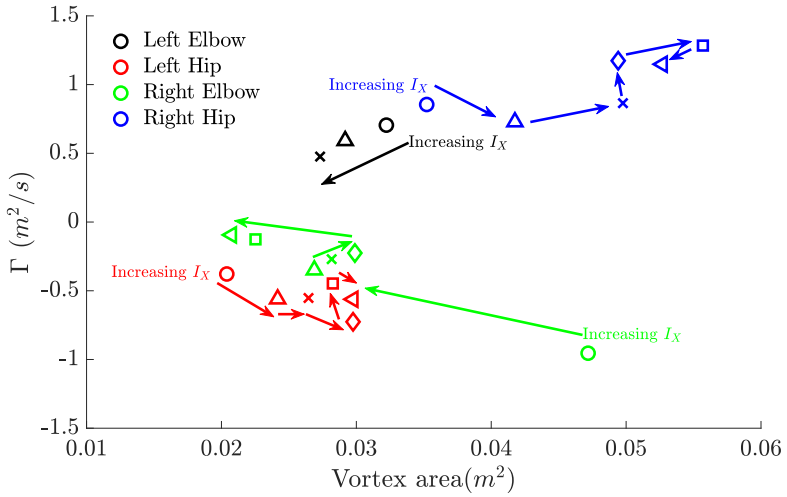


**Figure 12:** Vortex circulation, $\Gamma$ (m$^2$s$^{-1}$), versus vortex area (m$^2$) for the four key large-scale structures in the wake. The turbulence intensities, $I_x$, for each symbol are ○= 1.4 %, △= 2.5%, ×= 3.6%, ◇= 5.4%, □= 7.8%, and ◁ = 9.1%.

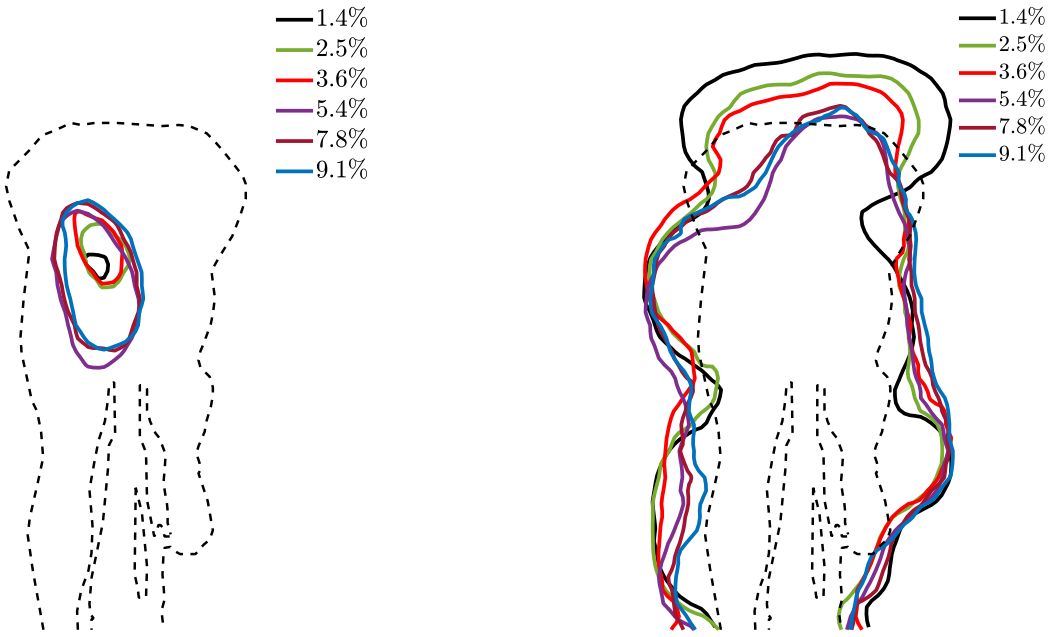


**Figure 13:** Velocity isolines behind the mannequin at a wind speed of 16 ms$^{-1}$ for **(a)** $W^* = 0.1$ and **(b)** $U^* = 0.9$.

wake deficit remains relatively similar to the lower turbulence case, with both the hip vortices coherent and having large velocity deficit areas. However, the lower wake, particularly from the outstretched left leg, changes from the $I_x = 2.4\%$ case. The isolines, $U^* = 0.9$ and $U^* = 0.8$, behind the left leg are close to the centre of the wake, and the associated vortices have disappeared or are significantly reduced in strength. It is probable that the increase in freestream turbulence causes an early onset to transition between the calf and the knee. This same transition was seen by Terra et al. (2020) for increasing Reynolds numbers, causing a similar effect to increasing freestream turbulence.

Increasing freestream turbulence to $I_x = 5.4\%$, results in a significant change in the global nature of the wake. This aligns with the large change in aerodynamic force presented in figure 8. The upper wake highlighted in figures 10(d) and 11(d) shows that no left elbow vortex is present and the associated velocity deficit region is no longer there. The $\Gamma_2$ criterion still identifies the right elbow vortex, although it is much weaker than for lower turbulence intensities. The reason that the elbow vortices disappear is discussed further in the section 3.2.5. The mid-wake profile associated with the two hip vortices has a reduced velocity deficit area with only a small region inside the isoline $U^* = 0.6$.

Interestingly, both the left and right hip vortex are significantly stronger. The left hip vortex has increased in strength by ~30% and the right hip by ~60%, based upon the circulation. Figure 13a shows isolines defining areas of high downwash, where the bounded area is $W^* (= \overline{w}/U_\infty) > 0.1$. Between $I_x = 3.6\%$ and $I_x = 5.4\%$, there is a significant increase of the area associated with downwash, increasing by a factor of $\sim 4$. It is proposed that this can be explained by: a) with no elbow vortices generating upwash, the flow will remain attached longer across the top of the back and be pulled into the large negative pressure in the wake; and b) a boundary layer transition through the hip region causing a later separation. As seen with increasing Reynolds numbers (Terra et al., 2020), a transition through the hip area elongates the recirculation region and increases the strength of the hip vortices formed. This coincides with the $C_L A\ (m^2)$ versus $Re$ measurements presented in figure 14, where lift-area is presented over a wind-speed range for each turbulence intensity case. The lift coefficient, in general, increases with increasing Reynolds number for all turbulence intensities. The increase in lift is likely caused by the change in the upper wake leading to significantly more downwash that in turn results in a larger lift-producing vortex pair. In the lower wake of the outstretched leg, the deficit region is reduced in size. One possible explanation for this change could be that the leg boundary layer transitions to the post-critical state leading to a much narrower wake. Due to varying changes in diameter across the leg, this will

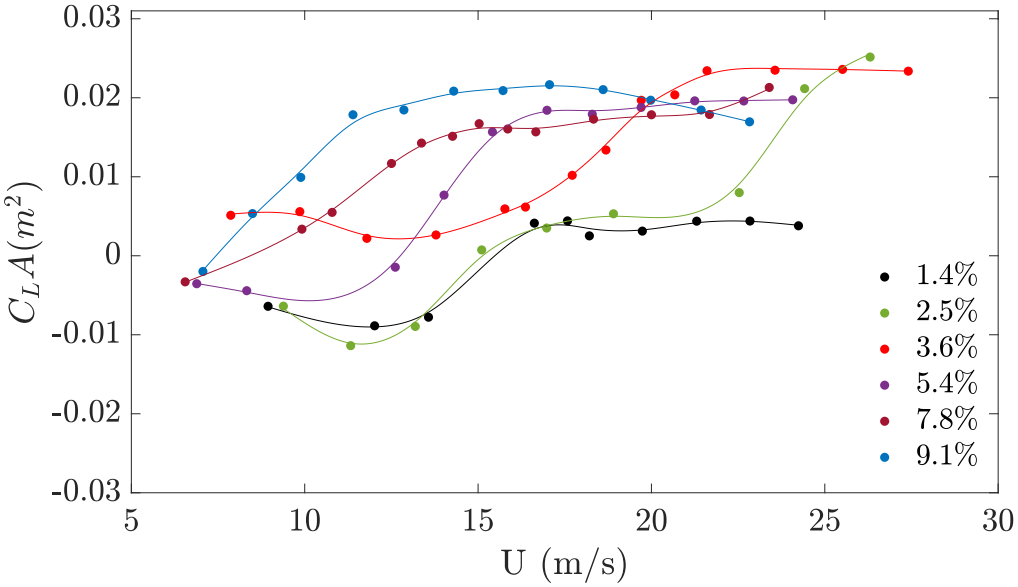


**Figure 14:** Lift area, $C_L A$ ($m^2$), against wind speed for turbulence intensities between 1.4% and 9.1%.

happen at different speeds due to varying local Reynolds numbers, considered further in section 3.2.5. All of the above discussion points help to explain the large reduction in $C_D A$ between $I_x = 3.6\%$ and $I_x = 5.4\%$ highlighted in figure 8.

Across the three highest turbulence intensities, $I_x = 5.4\%$, 7.8% and 9.1%, the wake profile is relatively similar. The left hip vortex strength peaks at $I_x = 5.4\%$, but remains relatively strong and of similar size across the three highest freestream turbulence levels. The right hip vortex is largest at $I_x = 7.8\%$, and then slightly reduces at $I_x = 9.1\%$. Figure 13a shows that $I_x = 5.4\%$ has the largest area of $w^* > 0.1$, which reduces in size as the $I_x$ is increased to 9.1%. The left elbow vortex reduces in strength with increasing $I_x$. Figure 13b shows the isoline of $U^* = 0.9$, which approximates the wake boundary. The upper wake vertical extent is at a minimum at $I_x = 5.4\%$ and subsequently grows larger over the left shoulder at the highest two freestream turbulence levels. This is likely due to the higher strength of the left hip vortex in the $I_x = 5.4\%$ case pulling the flow into the lower wake. The boundary of the wake behind the left outstretched leg changes across the highest three freestream turbulence levels. As turbulence intensity is increased, the wake width reduces. The outstretched leg has no upstream geometry interfering with the oncoming flow. Therefore, as the freestream turbulence is increased, the boundary layer over the leg undergoes earlier transition, resulting in delayed separation and a reduced wake size, similar to that seen for critical flow past a circular cylinder.

### *3.2.4. Total pressure grid profiles*

The time-averaged total pressure coefficient, $\overline{C}_P$, was measured over a range of wind speeds at each freestream turbulence level. This was possible because the required measurement time, for any particular configuration, was significantly lower than the traverse of the cobra probe, and therefore allowed for a wider range of cases to be considered. A baseline comparison of the total pressure grid-derived pressure coefficient and in-plane velocity contours at $I_x = 1.4\%$ and 16 $ms^{-1}$ is provided in figure 15. Figure 15(a) shows the $\overline{C_P}$ contour map, whereas figure 15(b) highlights the normalised streamwise velocity, $U^*$. It is clear that profiles are very closely aligned. The total pressure contours highlight two clear deficit regions within the wake that correlate with the hip and elbow vortices shed off the mannequin. The unsteady total pressure coefficient contour map shown in figure 15 is also comparable to that of the wake $\sigma_u/U_\infty$, both having distinct regions of fluctuations associated with the hip and elbow vortices. Further to this, figure 16 highlights two $\overline{C_p}$ contour maps for freestream turbulence of $I_x = 5.4\%$ at winds speeds of 10 $ms^{-1}$ and 20 $ms^{-1}$. Between 10 $ms^{-1}$ and 20 $ms^{-1}$, the upper wake total pressure deficit region reduces in size, similar to what was seen in 3.2.3 for the velocity profiles across each turbulence intensity. This shows increasing $Re$ at any given

freestream turbulence level can have a similar effect to increasing turbulence intensity. This result may explain the $C_DA$ versus wind speed variation (section 3.2.1), with the large reduction in $C_DA$ between 14 and 20 ms$^{-1}$.

Isolines of $\overline{C}_P$=0.9 across each turbulence intensity for a range of different wind speeds are shown in 17. This isoline is used to estimate the size and boundary of the wake. Figure 17a shows that for the baseline case, increasing the $Re$ has minimal effect on the boundary and shape of the wake. The two elbow vortices are present across the entire Reynolds number range, with the upper wake slightly reducing in size with increasing $Re$. This may explain the slight reduction in $C_DA$ with increasing $Re$. The lower wake maintains distinct boundaries. At $I_x = 2.5\%$, the boundary of the wake of the right hip has grown and shifted away from the body. At the highest speed of 24.3 ms$^{-1}$, not likely to be encountered by a competitive cyclist (except perhaps during downhill decents) but of academic interest regardless, the upper wake significantly reduces in size. As freestream turbulence increases, the reduction of the upper wake area occurs at lower wind speeds. This progression to a smaller upper wake is consistent with that seen in the wake velocity contour plots for increasing freestream turbulence examined previously. Therefore, we suggest the reduction in wake size is due to the reduction/suppression of strong elbow vortices off each arm resulting in a much smaller upper wake.

### *3.2.5. Flow visualisation*

Flow visualisation was conducted at the extreme turbulence levels of 1.4% and 9.1% to highlight the influence of background turbulence levels on the surface skin-friction distributions. All tests were conducted at a wind speed of 22 ms$^{-1}$. The figures below show China clay distributions after the evaporation of the kerosene mixture. The photos are taken under UV lighting to enhance the visualisation from the fluorescent pigments mixed with the China clay.

Figure 18a shows the left arm separation line from the elbow to the top of the shoulder. The Reynolds number based upon the average arm diameter is ~120 000. The separation line is not straight along the span of the arm as it deviates at the elbow joint. This is due to the variation in geometry across the span and the location of where the elbow vortex is formed. Figure 18b shows the surface flow visualisation across the arm for $I_x = 9.1\%$. It is evident that the separation line across the entire span of the arm has changed between the two freestream turbulence levels. At $I_x = 9.1\%$, the separation line has shifted towards the rear of the arm. This implies that the arm has undergone transition to the post-critical flow state.

Figure 19 shows the surface shear distributions of the torso and leg on both the left- and right-hand side of the mannequin for each turbulence intensity. It can be seen on the left-hand side of the torso there is a clear change in the distribution between $I_x = 1.4\%$ and $I_x = 9.1\%$. Figure 19a shows a clear channel without China clay along the torso of the mannequin. This may be the path of the elbow vortex as it hugs behind the arm and torso projecting into the upper wake. In figure 19b, the china clay is well distributed across the torso with the streamlines pulled to the hip region. This is consistent with the observation that the elbow vortex is no longer present in the downstream cross-plane once the arm has undergone boundary-layer transition.

Figures 19c and 19d show the surface distribution on the right-hand side of the body for the two turbulence intensities. It can be seen that the arm has undergone a boundary-layer transition similar to the left-hand side, with the separation point moving further downstream. In figure 19c, a similar channel to the left-hand side can be seen across the torso of the mannequin, although larger in size. This may be the path of the elbow vortex hugging the torso and projecting into the upper wake. This is consistent with the strength of the elbow vortices identified in the downstream velocity cross-plane with the left vortex having a larger size and circulation than the right. In figure 19d this channel is still present but reduced in size. Again, this is consistent with the velocity contour maps that identified that the right elbow vortex was still present, although significantly weaker in strength.

## *3.3. Skinsuit mannequin – 90 degree leg position*

This section considers the aerodynamic flows and forces over the mannequin fitted with a skinsuit, and configured in the 90-degree leg position. This will be referred to as the skinsuit configuration, and provides insight into the impact of turbulence when the surfaces are not smooth. Since the effects of upstream turbulence have similarities to surface roughness effects identified in previous studies, this provides a further useful comparison. It also allows the combined effects of turbulence and roughness to be quantified.

### *3.3.1. Force results*

The drag area, $C_DA$, as a function of wind speed, is shown in figure 20. For wind speeds 5 ms$^{-1}$ $< U_\infty <$ 12 ms$^{-1}$, all $C_DA$ curves show a montonically decreasing $C_DA$ with increasing speed. Beyond this initial behaviour, they reach

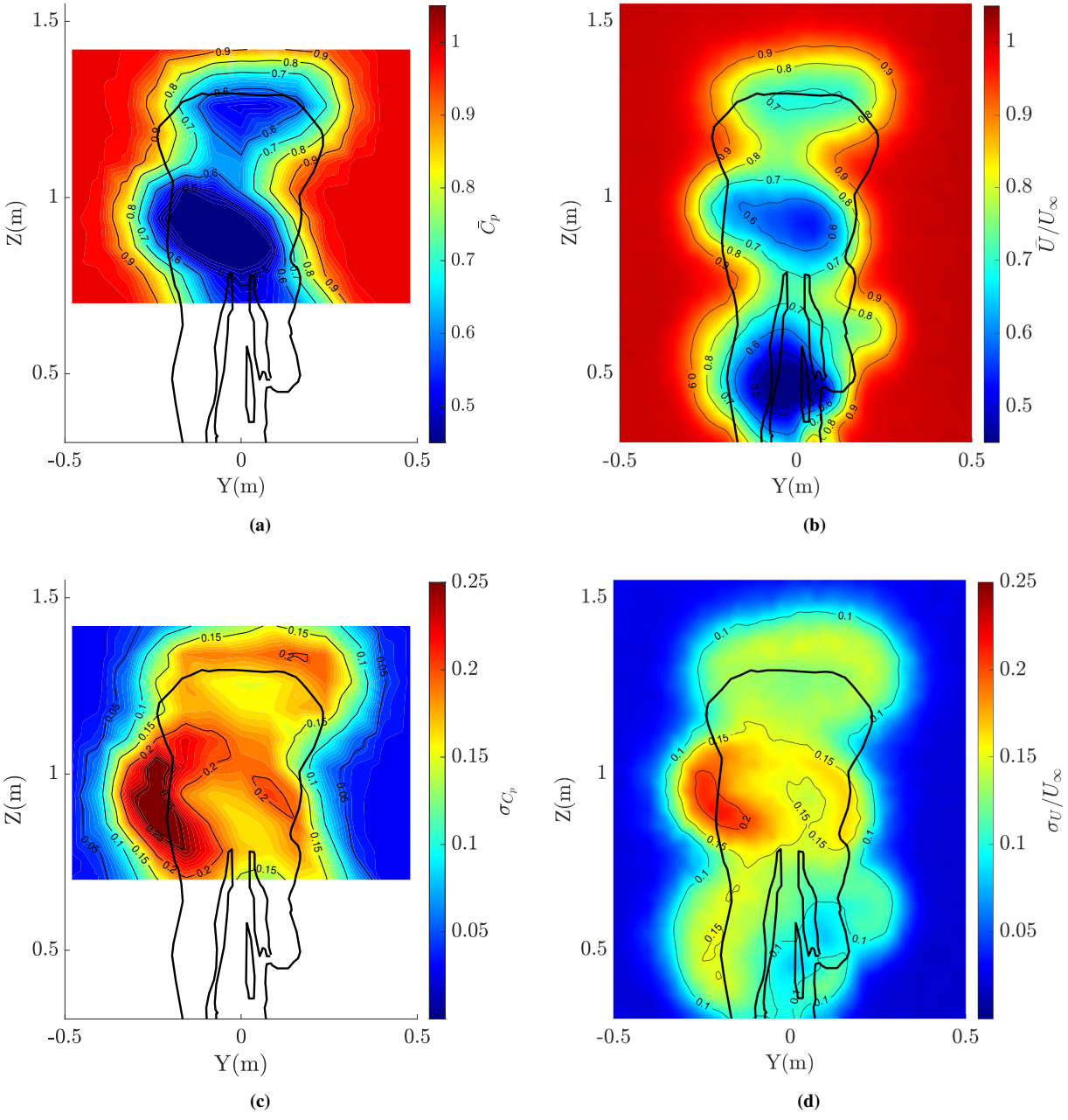


**Figure 15:** Wake contours of the bare mannequin at a wind speed of 16 ms$^{-1}$ for **(a)** total pressure coefficient, $C_P$, **(b)** normalized stream-wise velocity, $U^*$ **(c)** unsteady total pressure coefficient, $\sigma_{C_p}$, and **(d)** wake turbulence intensity, $\sigma_u/\overline{U}$.

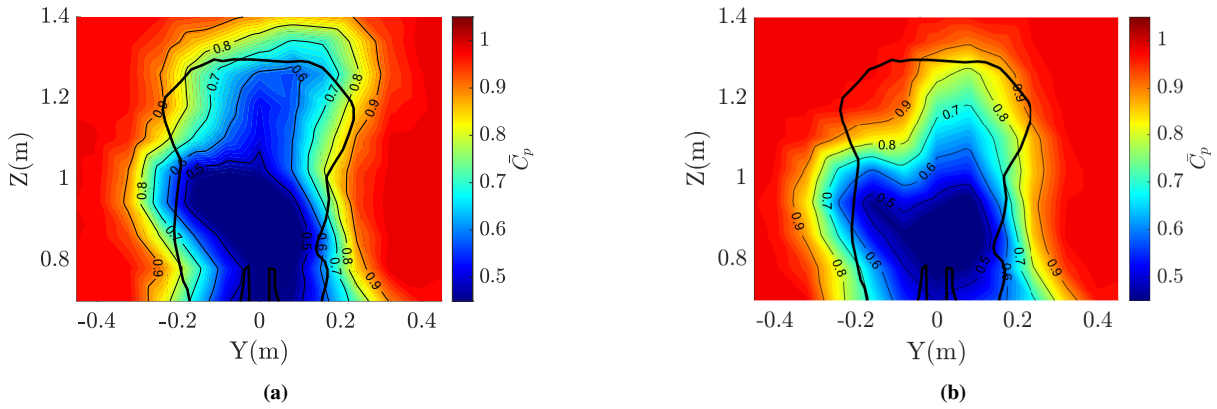


**Figure 16:** Total pressure coefficient contour maps for the bare mannequin for $I_x = 5.4\%$ at **(a)** 10 ms$^{-1}$ and **(b)** 20 ms$^{-1}$.

a minimum and bend upwards slightly. As $I_x$ is increased, the curves maintain a similar shape but are translated towards a lower wind speed. For each $I_x$, the minimum $C_DA$ occurs at the end of the approximately linear downward trend. As $I_x$ is increased from 1.4% to 3.6%, the minimum $C_DA$ reaches a smaller magnitude and occurs at a lower wind speed. Between $I_x = 7.8$ and 9.1%, the minimum $C_DA$ continues to occur at lower speeds, while its minimum value remains similar. Interestingly, when $I_x = 5.4\%$, the minimum $C_DA$ increases relative to the decreasing trend for the lower turbulence levels. For higher wind speeds after the minimum $C_DA$ is reached, generally there is a slow increase in drag-area with windspeed. This is the case for $I_x = 1.4\%$, 2.5%, 3.6%, 5.4% and 7.8%, while $C_DA$ remains approximately constant for $I_x = 9.1\%$.

Figure 21 compares the $C_DA$ of the bare and skinsuit configuration for each freestream turbulence intensity. For the baseline case of $I_x = 1.4\%$, the skinsuit has a positive effect on the aerodynamic performance of the mannequin when compared to the bare configuration. For this case, the $C_DA$ is reduced across the entire wind speed range tested when compared to the bare mannequin. At a typical race speed of 16 ms$^{-1}$, the skinsuit improves the aerodynamic performance with a 6.1% reduction in the drag area, $C_DA$. For $I_x = 2.5\%$ and 3.6%, the bare configuration begins to have a lower $C_DA$ at wind speeds $\gtrsim$ 20 ms$^{-1}$. Interestingly, the bare configuration outperforms the skinsuit mannequin for $I_x \gtrsim 5.4\%$ at typical race speeds ($>$ 13 ms$^{-1}$). For $I_x$ of 7.8% and 9.1%, the bare configuration is considerably better than the skinsuit configuration beyond $U \gtrsim 10$ ms$^{-1}$. An important point is that as wind speed increases, the skinsuit reaches a plateau to a relatively constant or slightly upward increasing $C_DA$, whereas the $C_DA$ for the bare mannequin continues to reduce substantially. For freestream turbulence levels of $I_x = 7.8\%$ and 9.1%, at a typical race speed of 16 ms$^{-1}$, the bare configuration's $C_DA$ is 5.7% and 9.8% lower than the skinsuit configuration, respectively.

### *3.3.2. Baseline wake topology – skinsuit*

A three-component velocity wake survey was conducted at the baseline freestream turbulence level, $I_x = 1.4\%$. Figure 22 shows normalised vorticity ($\omega_x$), and normalised wake velocity ($U^*$) contour maps of both the bare and the skinsuit configuration for the baseline case of $I_x$=1.4% for $U = 16$ ms$^{-}$. Fitting the mannequin with a skinsuit causes significant changes to the upper and middle sections of the wake. The upper wake deficit region reduces in size becoming narrower than for the bare mannequin. The introduction of roughness on the arms alters the left and right elbow vortex, which are both weaker in strength and have a reduced area. The Reynolds number of the arm of the mannequin is ~120 000, placing it on the border of the critical regime for a smooth circular cylinder. Previous studies have shown that the addition of roughness to a cylinder causes the transition to the post-critical flow state to occur at lower Reynolds numbers (Zdravkovich, 1990). Thus, it is reasonable to conclude that the addition of the targeted roughness to the arms of the skinsuit has caused the boundary layer to undergo transition to the post-critical flow state. Therefore, it can be assumed that we are seeing a similar effect on the wake to that seen with increasing levels of freestream turbulence. Interestingly, the boundary of the wake for the right elbow vortex is relatively large compared to the bare arm configuration, although the significant of this is unclear.

The mid-wake structures are similar to those of the bare configuration. The hip vortices are still the dominant

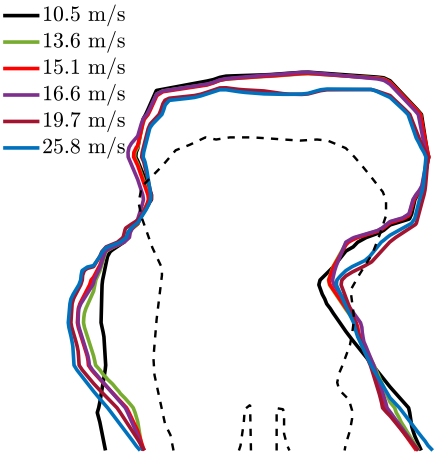


**(a)** $I_x = 1.4\%$

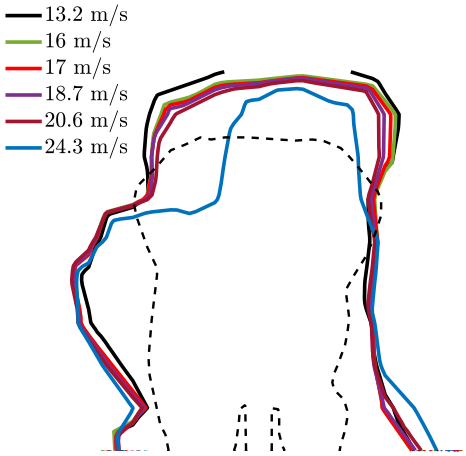


**(b)** $I_x = 2.5\%$

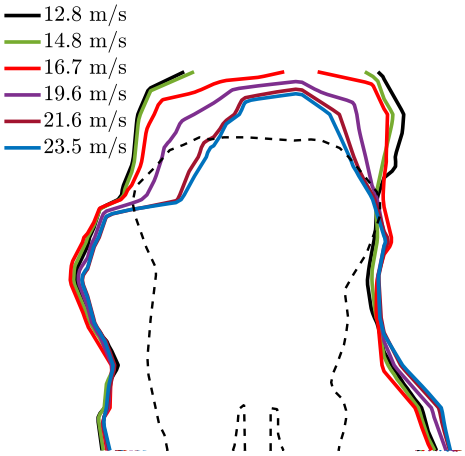


**(c)** $I_x = 3.6\%$

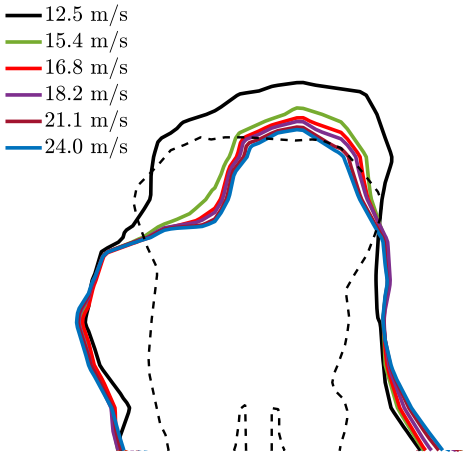


**(d)** $I_x = 5.4\%$

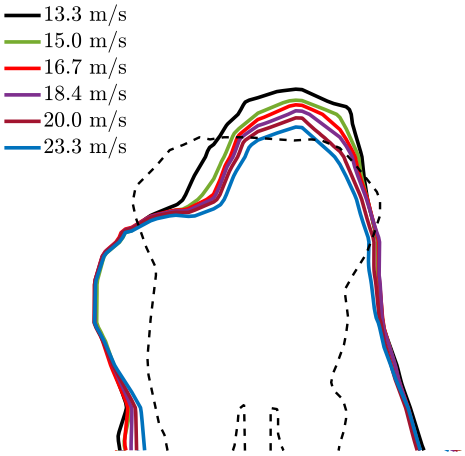


**(e)** $I_x = 7.8\%$

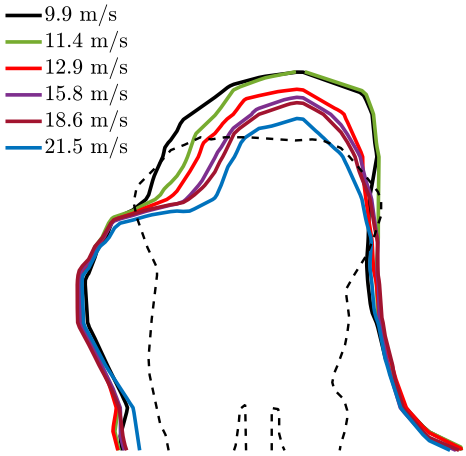


**(f)** $I_x = 9.1\%$

**Figure 17:** Line contours of $C_p = 0.9$ at different wind speeds, $U(\mathrm{ms}^{-1})$, in the wake of the bare mannequin in the $90^o$ leg position

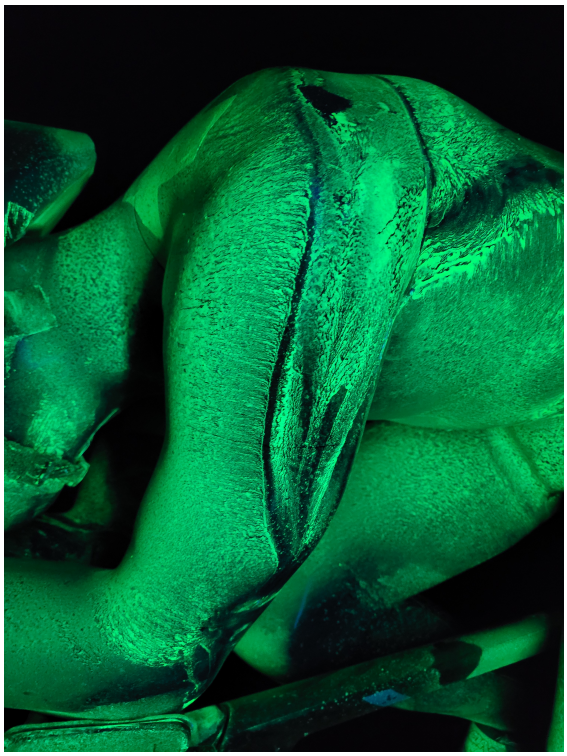

**(a)** $I_x = 1.4\%$

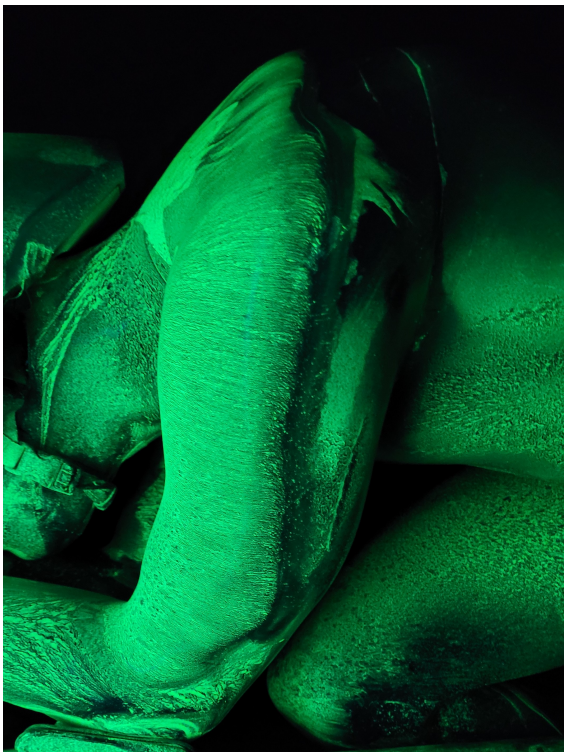

**(b)** $I_x = 9.1\%$

**Figure 18:** Images of the left arm surface streamlines under two different turbulent conditions.

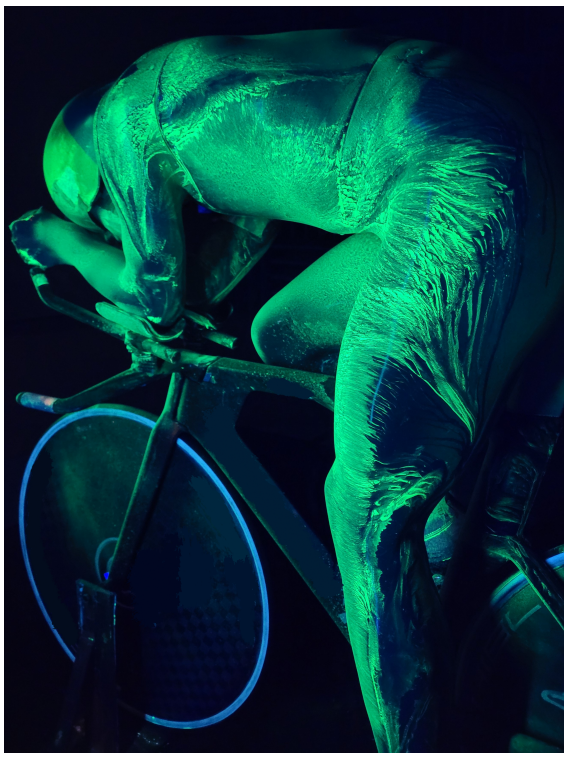

**(a)** LHS at $I_x = 1.4\%$

**(b)** LHS $I_x = 9.1\%$

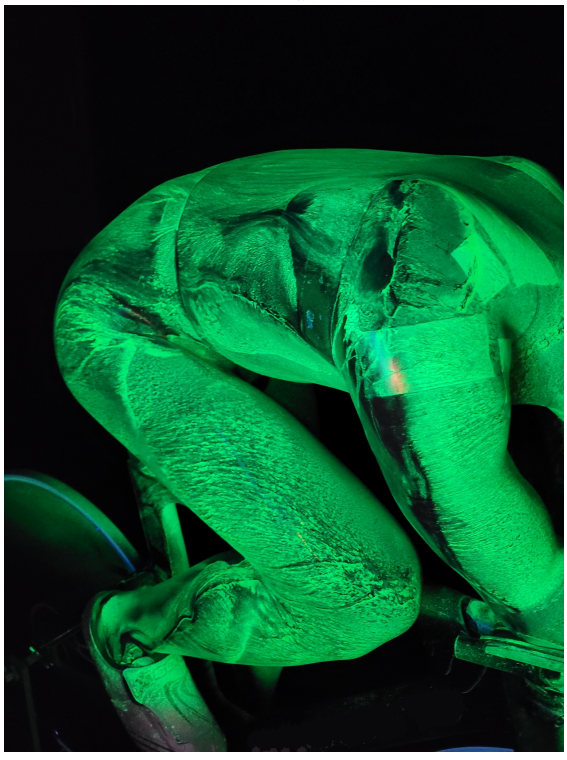

**(c)** RHS $I_x = 1.4\%$

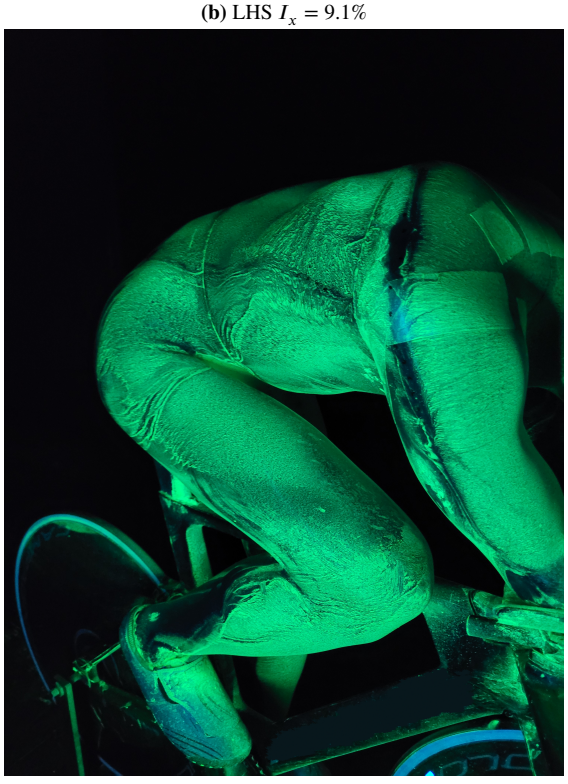

**(d)** RHS at $I_x = 9.1\%$

**Figure 19:** China clay distributions across the mannequin geometry for each turbulence intensity.

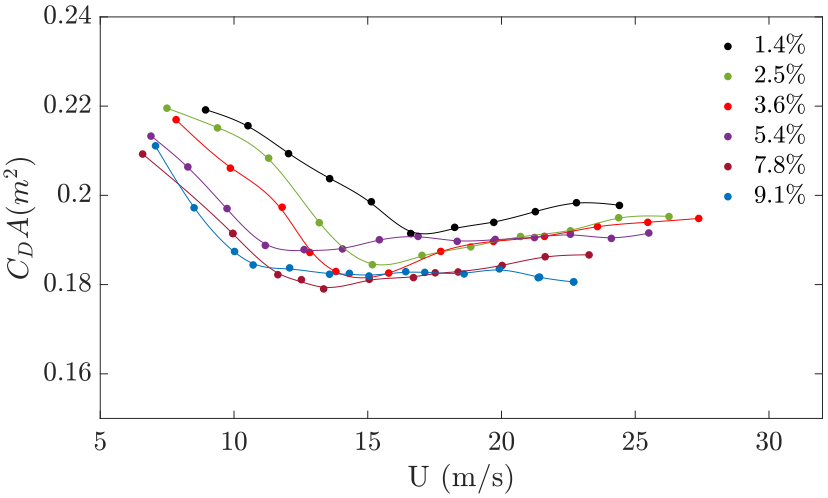


**Figure 20:** Drag area, $C_DA$ ($m^2$), versus wind speed for turbulence intensities between 1.4% and 9.1% for the mannequin wearing the skinsuit.

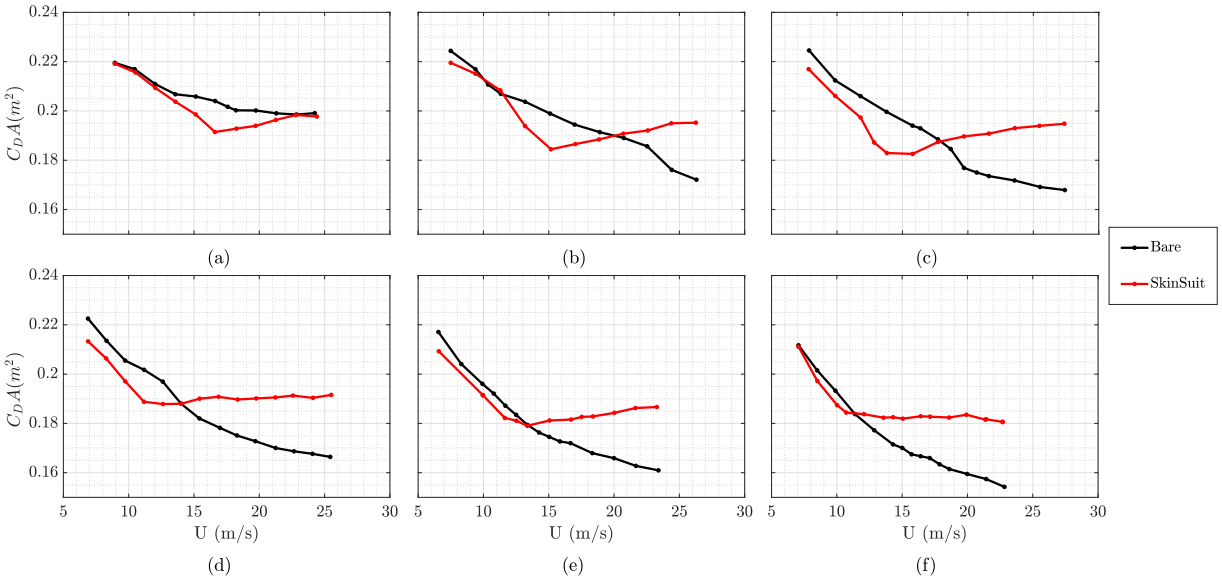


**Figure 21:** Drag area, $C_DA$ ($m^2$), against wind for skinsuit and bare configurations for **(a)** 1.4%, **(b)** 2.5%, **(c)** 3.6%, **(d)** 5.4%, **(e)** 7.8% and **(f)** 9.1%.

large-scale flow structures in the wake, and show slightly increased strength. The velocity contours show that the velocity deficit region has been compressed, elongated and rotated clockwise. The lower wake has changed in the region of the wake associated with the tucked right knee. The minor scale vortical structures have become a stronger counter-rotating pair, most likely shed off the right knee. This is likely to be from the presence of the Lycra material on the legs. However, the wake of the left outstretched leg is almost identical.

*3.3.3. Total pressure profiles – skinsuit*

Time-averaged total pressure coefficient contour lines of $C_P = 0.9$ across the wind-tunnel speed range and different turbulence configurations for the skinsuit configuration are shown in figure 23. This value of $C_P$ is used to (approximately) define the wake boundary. As the velocity is increased for each $I_x$, only small changes to the wake shape occur. Independent of $I_x$, the speed at which the minimum upper wake area occurs aligns with the minimum force value shown in figure 20. As $I_x$ is increased, the minimum upper wake area occurs at lower speeds. At that speed, the boundary of the wake behind the right hip is the largest and the upper wake is smallest. As speed is increased further, the size of the hip wake boundary is reduced and the upper wake area increased.

Across all turbulence levels, the wake of the left hip undergoes the least change. As $I_x$ is increased, the $C_P = 0.9$ boundary slightly increases in size, extending further away from the mannequin. The flow field associated with the hip region is highly three-dimensional and complex, as it is strongly influenced by upstream flow. At $I_x = 1.4\%$, the size and strength of the hip vortices increase with increasing $Re$ due to the nonlinear interaction with the transition and flow separation over the arms. It is proposed that the hip vortex continues to increase in strength with both increasing $I_x$ and wind speed, at least over the wind-speed range examined. Clearly, this point requires further experiments and analysis.

## 4. Conclusion

In this work, the influence of freestream turbulence on cycling aerodynamic performance was investigated through careful wind-tunnel experiments. This is, to our knowledge, the first systematic characterisation of these effects. The primary purpose was to quantify the changes to the aerodynamic drag of a cyclist and wake flow structures as the upstream turbulence level was varied. Importantly, this research identifies how highly sensitive the drag is to turbulence, with a drag reduction of up to 19% found for the highest turbulence level relative to the low turbulence case. This is a significant finding given the wide variety of environments a cyclist may experience, whether competing outdoors in a time trial (e.g., Le Tour de France) or in the turbulent wakes of competitors on-track. In both these cases, the turbulence intensity in likely to lie within the range considered in this study. It follows that an understanding of the turbulent environment can be as important to performance as the more often considered factors, such as cyclist speed and skinsuit surface structure. Therefore, prevailing conditions together with skinsuit design, equipment and positioning must be considered in combination to achieve optimal performance.

Three main sub-studies contributed to this overarching program: the examination of turbulence effects on the aerodynamics of a smooth mannequin at elite-cyclist racing speed; broadening this to consider the aerodynamics over a wind-speed range; and looking at the combined effects of surface roughness from clothing the mannequin in a skinsuit and turbulence intensity. The variation of the aerodynamic drag with wind speed (or equivalently cyclist speed through a still atmosphere) of the smooth mannequin was consistent with studies over generic bodies, such as circular cylinders and spheres. Increasing the level of turbulence reduced the drag-area of the mannequin, which is consistent with earlier boundary layer transition on surfaces such as the arms and legs leading to delayed separation and a reduced wake width. Indeed, the changes to the streamwise vortices in the wake could be attributed to significant changes to the flow over the arms and the legs of the mannequin.

When the boundary layer on either arm of the mannequin undergoes early transition there is a significant global wake change caused by the coupled interaction between the flow over the arm and onto the torso. In the near wake, 0.6 m from the rear of the cyclist, the circulation of the left elbow vortex reduces from 0.5 $ms^{-2}$ to essentially being undetectable, as the turbulence level is increased between 0–5%. Over this same turbulence intensity range, the right elbow vortex circulation also reduces in magnitude by a factor of 4. The overall result is that the extent of the upper wake reduce considerably in size. As this happens, both hip vortices increase in strength and size. The circulation of left and right hip vortices increases from 0.55 to 0.73 $m^2s^{-1}$, and from 0.86 to 1.18 $m^2s^{-1}$, respectively. Given that the

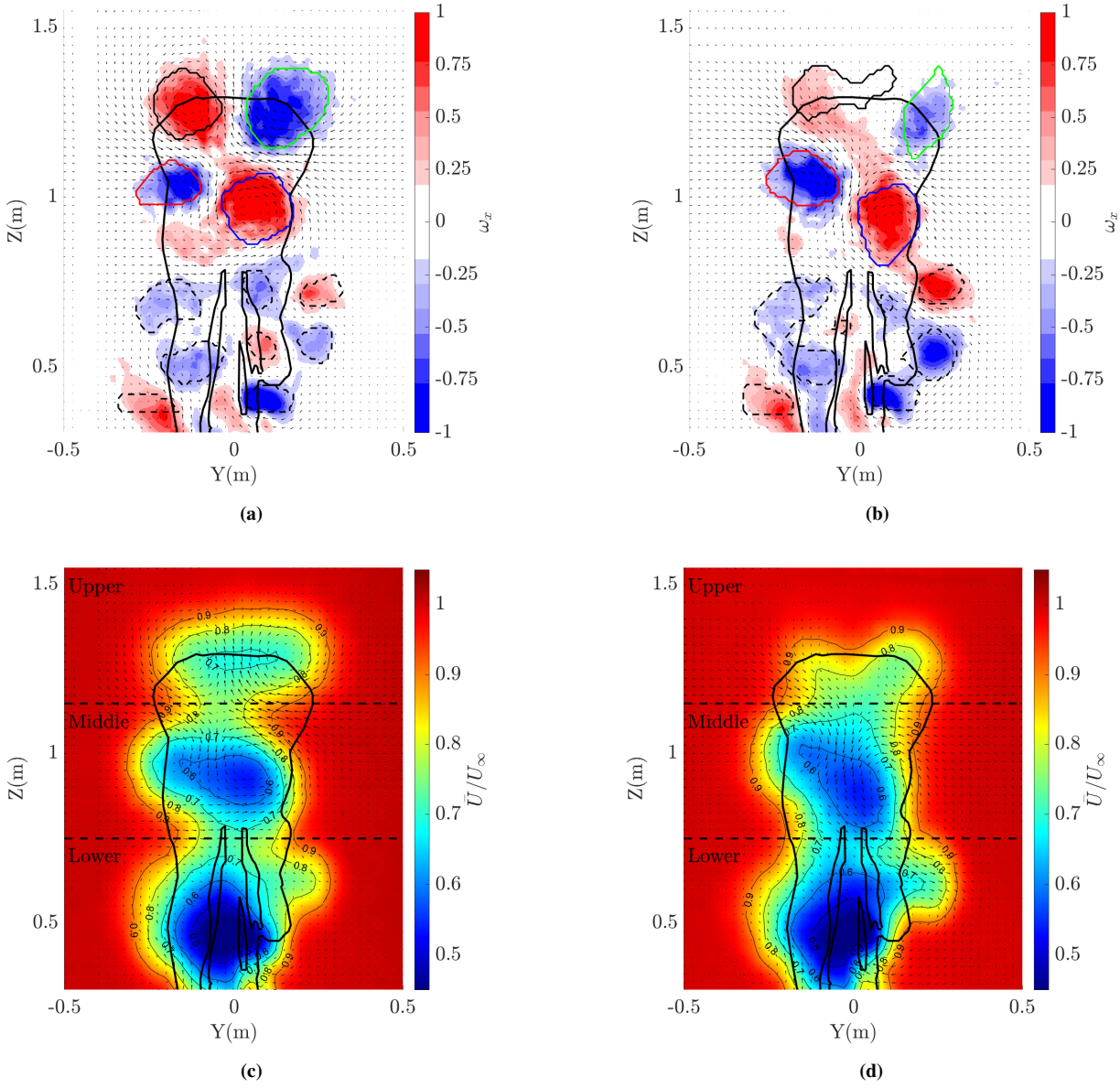


**Figure 22:** Wake contour maps at 0.6 m behind the mannequin for the baseline case of $I_x = 1.4\%$ showing normalized vorticity, $\omega_x$ for **(a)** the bare mannequin and **(b)** the skinsuit configuration, and normalised velocity contours of $U^*$ for **(c)** the bare mannequin and **(d)** the mannequin with the skinsuit. Key large-scale structures identified with different part of the geometry have been highlighted. The different lines correspond to: —·- = left elbow, — = right elbow, — = left hip, —·- = right hip, – – = lower wake structures. The wind-tunnel flow speed is 16 ms$^{-1}$.

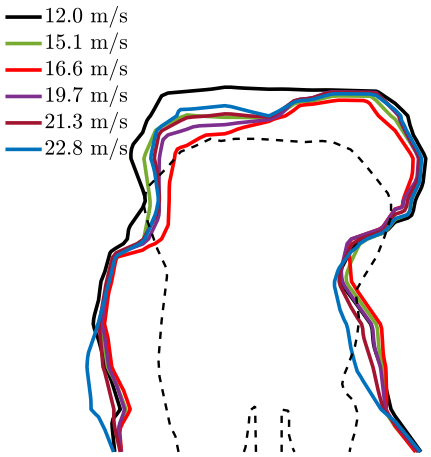


**(a)** $I_x = 1.4\%$

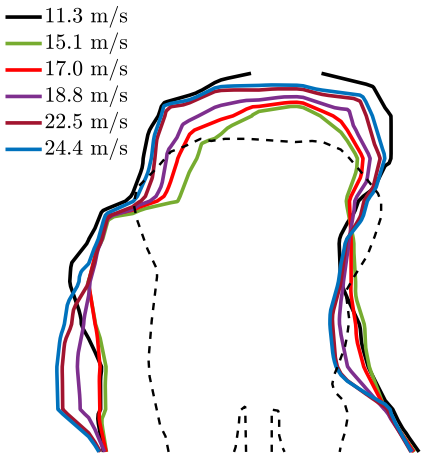


**(b)** $I_x = 2.5\%$

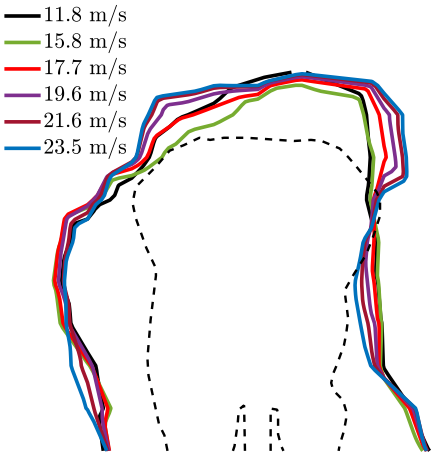


**(c)** $I_x = 3.6\%$

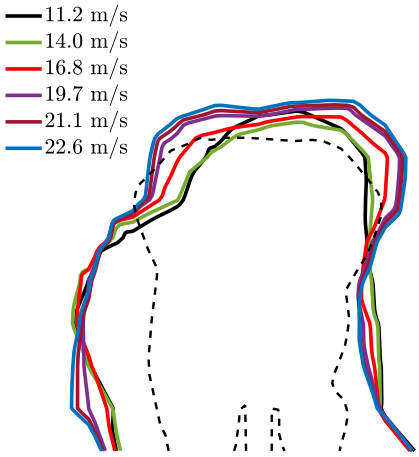


**(d)** $I_x = 5.4\%$

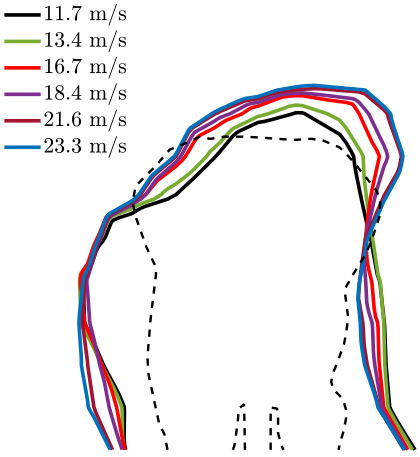


**(e)** $I_x = 7.8\%$

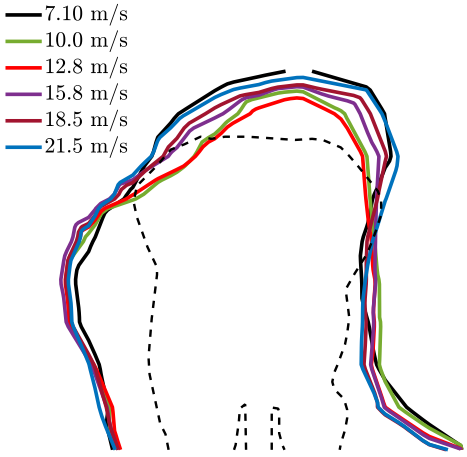


**(f)** $I_x = 9.1\%$

**Figure 23:** Line contours of $C_p = 0.9$ at different wind speeds, $U(\text{ms}^{-1})$, in the wake of the mannequin in the $90^o$ leg position wearing the Lyrca skinsuit across each $I_x$.

elbow and hip vortices are dominant streamwise structures for the low turbulence case, this is an important change to the global wake and can be connected back to the reduction in the drag (up to 8.3%). This occurs at an arm-width-based Reynolds numbers of $\sim 120\,000$, with increasing freestream turbulence level.

For the mannequin dressed in a skinsuit, the surface texture on the arms of the mannequin causes the boundary layer to undergo transition at a lower Reynolds number, a well-known phenomenon seen on circular cylinders as the surface is roughened. In combination, the critical Reynolds number decreases with increasing levels of turbulence. The minimum $C_d A$ slightly reduces as turbulence is increased. Once the boundary layer on the arms undergoes transition, the overall near-wake cross-sectional size increases with increasing turbulence levels, an opposite behaviour to that seen for the smooth case. It is hypothesised that the roughness of the Lycra material restricts the flow behaviour within the hip regions. This is an important conjecture, as placing roughness on the arms is now standard practice for professional riders, and often the remainder of the skinsuit is designed more for rider comfort. This suggests that the aerodynamic performance of a skinsuit is susceptible to not only to the type of roughness used on the arms but also the remaining surface texture over the rest of the skinsuit.

Finally, another interesting outcome is while the effects of background turbulence and (localised) skinsuit texture appear similar, in that they can lead to a lowering of drag and earlier onset of post-critical flow, there also appear to be some differences. In particular, the overall drop in drag coefficient as the speed is increased caused by surface roughness seems to reach a minimum and then plateau or slightly increase. As turbulence level is increased, the minimum tends to occur at lower speeds and is deeper. On the other hand, for the bare (smooth) mannequin, increasing speed up to 25 $\mathrm{ms}^{-1}$ results in a steadily monotonic lowering of drag coefficient over the entire speed range with no indication of reaching a minimum value. This leads to considerably lower drag than achievable through skinsuit roughness applied to the arms. For background turbulence levels beyond 5%, the bare mannequin provides an aerodynamic advantage at typical elite racing speeds ($> 14$ $\mathrm{ms}^{-1}$), with this cross-over point reducing as turbulent level is increased. This further highlights the importance of understanding the environment in which athletes compete and its interaction with other drag-reduction measures.

## References


Springer handbook of experimental fluid mechanics. *American Institute of Aeronautics and Astronautics. AIAA Journal*, 46(10):2653, 2008. ISSN 0001-1452.

E. Achenbach. Distribution of local pressure and skin friction around a circular cylinder in cross-flow up to $Re = 5 \times 10^6$. *Journal of Fluid Mechanics*, 34:625–639, 1968.

E. Achenbach. Influence of surface roughness on the cross-flow around a circular cylinder. *Journal of Fluid Mechanics*, 46:321–355, 1971.

T. Avadiar, M. C. Thompson, J. Sheridan, and D. Burton. The influence of reduced Reynolds number on the wake of the D]rivAer estate vehicle, journal = Journal of Wind Engineering and Industrial Aerodynamics, volume = 88, pages = 207-216, year = 2019, type = Journal Article.

N. Barry, D. Burton, , J. Sheridan, M. C. Thompson, and N. A. T. Brown. Aerodynamic performance and riding posture in road cycling and triathlon. *Proceedings of the Institution of Mechanical Engineers, Part P: Journal of Sports Engineering and Technology*, 229(1):28–38, 2015a.

N. Barry, D. Burton, , J. Sheridan, M. C. Thompson, and N.A.T. Brown. Aerodynamic drag interactions between cyclists in a team pursuit. *Sports Engineering*, 20:81–110, 2015b.

P.W. Bearman and T. Morel. Effect of free stream turbulence on the flow around bluff bodies. *Progress in Aerospace Sciences*, 20(2):97–123, 1983. ISSN 0376-0421.

J. Bell, D. Burton, M. C. Thompson, A. Herbst, and J. Sheridan. Dynamics of trailing vorticies in the wake of a generic high seed train. *Journal of Fluids and Structures*, 96:238–256, 2016.

H. M. Blackburn and W. H. Melbourne. The effect of free-stream turbulence on sectional lift forces on a circular cylinder. *Journal of Fluid Mechanics*, 306:269–292, 1996.

B. Blocken, Y. Toparlar, T. van Druenen, T. Adrianne, T, T. Marchal, G. Maas, and J. Diepens. Aerodynamic drag in cycling pelotons: New insights by CFD simulation and wind tunnel testing. *Journal of Wind Engineering and Industrial Aerodynamics*, 179:319–337, 2018.

C. Brown, T. Crouch, D. Burton, and M. C. Thompson. Understanding the aerodynamic benefits of drafting in the wake of cyclists. *Proceedings*, 49:32, 2020.

L. Brownlie, C. Kyle, J. Carbo, N. Demarest, E. Harber, R. MacDonald, and M. Nordstrom. Streamlining the time trial apparel of cyclists: The Nike swift spin project. *Sports Technology*, 2(1-2):53–60, 2009.

D. Burton, S. Wang, D. Tudball Smith, H. N. Scott, T. N. Crouch, and M. C. Thompson. The influence of background turbulence on Ahmed-body wake bistability. *Journal of Fluid Mechanics*, 926:R1, 2021. doi: 10.1017/jfm.2021.706.

T. N. Crouch, D. Burton, N. A. T. Brown, and M. C. Thompson. Flow topology in the wake of a cyclist and its effect on aerodynamic drag. *Journal of fluid mechanics*, 748:5–35, 2014.

T. N. Crouch, D. Burton, M. C. Thompson, N. A. T. Brown, and J. Sheridan. Dynamic leg-motion and its effect on the aerodynamic performance of cyclists. *Journal of fluids and structures*, 65:121–137, 2016.

T. N. Crouch, D. Burton, M. C. Thompson, N. A. T. Brown, and J. Sheridan. Riding against the wind: A review of competition cycling aerodynamics. *Sports Eng*, 20:81–110, 2017.

T. Defraeye, B. Blocken, E. Koninckx, P. Hespel, P. Verboven, B. Nicolai, and J. Carmeliet. Cyclist drag in team pursuit: Influence of cyclist sequence, stature, and arm spacing. *Journal of Biomechanical Engineering*, 136, 2014.

S. Fitzgerald, R. Kelso, P. Grimshaw, and A. Warr. Measurement of the air velocity and turbulence in a simulated track cycling team pursuit race. *Journal of Wind Engineering  Industrial Aerodynamics*, 190, 2019.

S. Fitzgerald, R. Kelso, P. Grimshaw, and A. Warr. Measurements of roll, steering, and the farfield wake in track cycling. *Scientific reports*, 190, 2022.

L. Graftieaux, M. Michard, and N. Grosjean. Combining piv, pod and vortex identification algorithms for the study of unsteady turbulent swirling flows. *Measurement Science and Technology*, 12:1422–1429, 2001.

J. C. R. Hunt, Wray A. A., and Moin P. Eddies, streams, and convergence zones in turbulent flows. In *Center for Turbulence Research Proceedings of the Summer Program, Center for Turbulence Research*, pages 193–208, 1988.

C. Jux, A. Sciacchitano, J. Schneiders, and F. Scarano. Robotic volumetric piv ofăaăfull-scale cyclist. *Experiments in fluids*, 18:1–10, 2018.

I. Khabbouchi, H. Fellouah, M. Ferchichi, and M. S. Guellous. Effects of free-stream turbulence and Reynolds number on the separated shear layer from a circular cylinder. *Journal of Wind Engineering and Industrial Aerodynamics*, 135:46–56, 2014.

S. Kwangmin, C. Jin, J. Woo-Pyung, and C. Haecheon. Effect of free-stream turbulence on the flow over a sphere. *Physics of Fluids*, 22, 2010.

E. Mercker, G. Wickern, and J. Weidemann. Contemplation of nozzle blockage in open jet wind-tunnels in view of different 'Q' determination techniques. *SAE technical paper series*, 1997. ISSN 0148-7191.

W. Z. Sadeh and D. B. Saharon. Turbulence effect on crossflow around a circular cylinder at subcritical Reynolds numbers, 1982.

W. Terra, A. Sciacchitano, and Y.H Shah. Cyclist Reynolds number effects and drag crisis distribution. *Journal of Wind Engineering and Industrial Aerodynamics*, 200, 2020.

T. von Kármán. Progress in statistical theory of turbulence. *Proceedings of the National Academy of Sciences of the United states of America*, 31: 530, 1948.

S. Wang, J. Pitman, C. Brown, D. Tudball Smith, T. Crouch, M. C. Thompson, and D. Burton. The influence of the inter-relationship of leg position and riding posture on cycling aerodynamics. *Fluids*, 7(1), 2022.

S. Wordley and J. Saunders. On-road turbulence. *SAE International Journal of Passenger Cars – Electronic and Electrical Systems*, 1:341–360, 2009.

M. M. Zdravkovich. Conceptual overview of laminar and turbulent flows past smooth and rough circular cylinders. *Journal of Wind Engineering and Industrial Aerodynamics*, 33:567–581, 1990.